Published in final edited form as:
Nat Genet. 2022 September ; 54(9): 1376–1389. doi:10.1038/s41588-022-01159-z.

The genomic landscape of pediatric acute lymphoblastic leukemia

A full list of authors and affiliations appears at the end of the article.

Abstract

Acute lymphoblastic leukemia (ALL) is the most common childhood cancer. Here, using whole genome, exome and transcriptome sequencing of 2,754 childhood ALL patients, we find that despite a generally low mutation burden, ALL cases harbor a median of 4 putative somatic driver alterations per sample, with 376 putative driver genes identified varying in prevalence across ALL subtypes. Most samples harbor at least one rare gene alteration, including 70 putative cancer driver genes associated with ubiquitination, SUMOylation, non-coding transcripts and other functions. In hyperdiploid B-ALL, chromosomal gains are acquired early and synchronously, prior to ultraviolet-induced mutation. By contrast, ultraviolet-induced mutations precede copy gains in B-ALL cases with intrachromosomal amplification of chromosome 21 (iAMP21). We also demonstrate prognostic significance of genetic alterations within subtypes. Intriguingly, *DUX4*- and *KMT2A*-rearranged subtypes separate into *CEBPA/FLT3*- or *NFATC4*-expressing subgroups with potential clinical implications. Together, these results deepen understanding of the ALL genomic landscape and associated outcomes.

Introduction

Acute lymphoblastic leukemia (ALL) arises from B- or T-lineage lymphoid progenitors and is the most common childhood cancer, and is comprised of over 30 genetically distinct subtypes of prognostic importance[1,2]. Previous studies have identified subtypes and secondary mutations that influence risk stratification and prognosis (e.g. *IKZF1*

Reprints and permissions information is available at www.nature.com/reprints.

Correspondence: Charles G. Mulligan, Department of Pathology, 262 Danny Thomas Place, MS342, St Jude Children's Research Hospital, Memphis, TN 38105, charles.mullighan@stjude.org; Jinghui Zhang, Department of Computational Biology, 262 Danny Thomas Plac, St Jude Children's Research Hospital, Memphis, TN 38105, jinghui.zhang@stjude.org; Stephen P. Hunger, Children's Hospital of Philadelphia, Colket Translational Research Building, Room 3060, 3501 Civic Center Blvd, Philadelphia, PA 19104, Hungers@chop.edu, **Correspondence and requests for materials** should be addressed to S.P.H., J.Z. and C.G.M.

[¶]Deceased

[*]These authors contributed equally.

[**]These authors jointly supervised this work

Authorship contribution

Contribution: S.W.B. genomic data analysis, data interpretation and manuscript writing. K.G.R. study design, sample preparation, data interpretation and manuscript writing. Z.G., L.S., S.P., C.Q., X.M., L.W., S.A., K.H., Y.L., B.X., D.A.F., O.P., C.R., Y.L., M.P., X.C., Y.L., Y.F., J.R.M., M.R., M.R.W., S.F., D.H., S.Ne, X.Z., J.W., E.S., S.R., V.P., G.W., A.E., and E.R., data analysis. D.P. and C.C., statistical analysis. A.N.H. and D.P-T., sample preparation. I.I. and P.B., sample preparation and experimental work. M.J.B. and B.L.W. reviewed flow cytometry. Y.D., M.D., S.C.R., J.G-F., J. G-A., P.G., M.A.S., N.W., A.J.C., N.A.H., R.C.H., C.L.W., E.L., E.A.R., W.L.C., P.A.Z-M., K.R.R., L.A.M., K.W.M., S.S.W., M.J.B., W.S., K.P.D., A.A., K.C., J.R.D., S.J., C-H.P., W.E.E., J.Y., M.V.R., D.S.G., M.L.L., and S.P.H., patient samples and clinical data. J.Z. data interpretation and manuscript writing. C.G.M. designed and oversaw the study, data interpretation and manuscript writing.

Extended data is available for this paper.

Supplementary Information is available for this paper.

alterations[3,4], Ph-like ALL[5,6], *DUX4*[7,8], *MEF2D*[9], *ZNF384*-rearranged ALL[10,11], PAX5 P80R[12,13] and PAX5alt[14,15] ALL)[16,17]. Many of these studies have examined small cohorts, lacked genome-wide analysis, or have had limited integration of RNA and DNA sequencing. Here we performed an integrated multiplatform genomic analysis of 2,754 cases of pediatric ALL to identify new putative cancer driver genes, and to define the spectrum, co-occurrence, clonality, sequence of acquisition and prognostic importance of germline and somatic genetic alterations across the landscape of B- and T-ALL.

Results

Patient cohort and genomic sequencing

We studied 2,754 children, adolescents and young adults (AYA) with newly diagnosed B-ALL (n=2,288 cases) or T-ALL (n=466) (Supplementary table 1 and Extended data fig. 1). Median age at diagnosis was 6.4 years (range 0.08 – 30.7), with 58.2% male and 41.8% female (Supplementary table 2). The cohort comprised 1,209 childhood National Cancer Institute (NCI) standard-risk (SR, 43.9%; age range 1-9.99 years, white blood cell count (WBC) ≤ 50,000/µl), 1,252 childhood NCI high-risk (HR, 45.5%; age range ≥10 to 15.99 years and/or WBC > 50,000/µl) and 275 AYA patients (10.0%; age range 16-30.7 years). Genomic analyses were performed using paired tumor and normal samples derived from bone marrow or peripheral blood obtained at leukemia remission for whole exome sequencing (WES; n=1,729), whole genome sequencing (WGS; n=768), and single nucleotide polymorphism array (SNP; n=1,808). Tumor-only whole transcriptome sequencing (RNA-seq) was performed on 1,889 patients (Extended data fig. 1).

Mutation burden differs across ALL molecular subtypes

B-ALL cases were classified into 24 different molecular groups[18] and T-ALL into 10 groups[17,19], with significant differences in genomic subtype between T-ALL and early T cell precursor (ETP) ALL (Fig. 1a, Extended data Fig. 2–3 and Supplementary table 2). In cases with WES and/or WGS (n=2141; Extended data Fig. 4a), we identified 24,199 somatic nonsynonymous single-nucleotide variants (SNVs; median 9 nonsynonymous SNVs per sample, range 0-269) and 3,314 somatic coding-region insertion/deletion mutations (indels; median 1 indel per sample, range 0-34) in 10,404 genes (median 10 genes per sample, range 0-252; Supplementary table 3). In cases with WGS, we identified 15,715 somatic structural variants (SVs) genome wide (median 15 SVs per sample, range 0-115; Supplementary table 4) and in cases with RNA-seq and/or WGS (n=2,049) we identified 1,301 somatic putative driver gene rearrangements (Supplementary table 5).

Overall, the median somatic mutation rate in ALL was 0.35 SNVs per megabase (Mb), which in B-ALL ranged from 0.15 in the *KMT2A*-rearranged subtype to 0.66 in iAMP21 (Fig. 1b), and in T-ALL from 0.28 in *TAL2* to 0.55 in *NKX2-1* (Fig. 1c). Overall, 376 putative driver genes were identified using the mutation-significance detection tools MutSigCV (SNVs and indels)[20], GRIN (SNVs, indels and copy number alterations (CNAs); Supplementary table 6)[21], GISTIC (CNAs)[22] and Medal Ceremony[23]; 70 of which were not previously reported in ALL (Extended data fig. 4b, Supplementary table 6). Of these 70 putative drivers, 43 have been reported in other solid or hematological tumors but not

ALL, and 27 had not been previously reported as targets of somatic alteration in human malignancies[24,25]. The median number of somatic putative driver gene alterations identified per case (including SNVs, indels, focal deletions, and fusions/rearrangements) was 4 (range 0-19) (Fig. 1b, c), similar to the number identified in adult cancers[26]. Putative driver CNAs (focal deletions) were more prevalent in B-ALL (median 2 (range 0-18) for B-ALL vs. 1 (0-6) for T-ALL, P=8.98x10^{-18} by two-sided t-test), whilst putative driver SNVs/indels were more frequent in T-ALL (1 (0-8) for B-ALL vs. 3 (0-11) for T-ALL, P=4.82x10^{-54}). In B-ALL, the number of putative driver alterations per case was the highest in Ph-like-*CRLF2*, Ph-like-other, and iAMP21 subtypes (mean 7.6, 6.8, and 6.5 alterations) and lowest in low hypodiploid and *KMT2A*-rearranged ALL (2.0 and 2.1; Fig. 1b). In T-ALL, the *TLX3* and *TLX1* deregulated subtypes had the highest putative driver burdens (8.0 and 7.8) while *TAL1* and *TAL2* had the lowest (4.8; Fig. 1c). In B-ALL, only 2.2% of samples had no detected putative driver gene alterations (most in hyperdiploid B-ALL). A putative driver gene alteration was detected in every T-ALL sample.

Contrasting patterns of mutational signatures in ALL

Mutational signatures were compared across ALL subtypes using WGS (Fig. 1b, c and Supplementary tables 7–8)[27]. COSMIC signatures 1 and 5 (clock-like cell-intrinsic processes)[28] were present in almost all samples (100% and 98%, respectively) and these signatures' mutation burden positively correlated with age in more than half of the subtypes (Extended data fig. 5a, b). Signatures 2 and 13 (APOBEC) were enriched in *ETV6-RUNX1* and *ETV6-RUNX1*-like B-ALL (detected in 43% and 100% of samples, respectively; Fig. 1b)[24]. Signature 7 (UV) was enriched in cases with gross chromosomal alterations, including hyperdiploid (detected in 17% of samples), near haploid (35%) and iAMP21 B-ALL (46%; Fig. 1b). Unexpectedly, we observed enrichment of signature 18 (ROS) in several subtypes including Ph-like-*CRLF2* (detected in 21% of samples), Ph-like-other (11%), and PAX5alt (41%) B-ALL, and *TAL1* (36%) and *LMO1/2* (67%) in T-ALL (Fig. 1b, c). The APOBEC and UV signatures did not increase with age, consistent with episodic[29] or environmental mutagenesis (Extended data fig. 5c, d). By contrast, the ROS signature increased with age in several subtypes, suggesting a constant cell-intrinsic process (or alternatively, a sustained environmental exposure), and was associated with 20q and 9p deletions in Ph-like-*CRLF2* (P = 1.5 x 10^{-5} and P = 5.1 x 10^{-5}, respectively, by Fisher's exact test) Ph-like-other (P = 8.5 x 10^{-4} and P = 8.5 x 10^{-4}), and PAX5alt (P = 0.013 and P = 0.048; Extended data fig. 5e, right).

Evolution of mutations and aneuploidy in B-ALL

Hyperdiploid ALL is the most common subtype of childhood leukemia, but the timing of acquisition of the aneuploidies and sequence mutations is unknown. We used regions with triploid chromosomes as a molecular clock to assess whether UV-induced SNVs preceded the copy number gain (present on 2 of 3 or 1 of 3 chromosomal copies), or occurred after the gain (present exclusively on 1 of 3 chromosomal copies; Fig. 2a). UV-induced SNVs were found on only 1 of 3 triploid chromosomes (variant allele frequency (VAF) ≈ 0.33; Fig. 2b) in hyperdiploid B-ALL[24], consistent with copy gains occurring early, potentially in utero[30], as they preceded UV exposure.

Four scenarios of ploidy evolution were observed in hyperdiploid ALL (Fig. 2c–d). The most common pattern was synchronous early chromosomal gains with somatic SNVs predominantly on 1 of 3 trisomic chromosomes, indicating that copy gains temporally preceded point mutations (83.6% of hyperdiploid samples). Second, we observed a synchronous late pattern in which all copy gains occurred late, as evidenced by mutations present on 2 of 3 trisomic chromosomes (VAF ≈ 0.67, 1.4% of samples). Finally, we observed asynchronous gain with most whole-chromosome copy gains early and (a) one late chromosomal arm gain (6.9%) or (b) one late whole chromosome gain (5.5%) (Fig. 2d, Extended data fig. 6 and Supplementary table 9). The predominance of somatic mutations on 1 of 3 copies (indicating early copy gains) was not simply due to the later UV mutational signature, since even hyperdiploid B-ALLs bearing only clock-like signatures 1 and 5 primarily had the synchronous early pattern of copy gains (88.4% of samples).

By contrast, in iAMP21, UV-associated mutations occurred prior to most chromosomal gains, as demonstrated by the presence of UV-induced SNVs on both 1 of 3 and 2 of 3 trisomic regions (Fig. 2b, Supplementary table 10)[24]. These findings are consistent with the notion of a chromosomal “big bang” early event in the evolution of hyperdiploid ALL, with simultaneous acquisition of trisomies prior to mutational evolution; by contrast, iAMP21 is characterized by repetitive breakage-fusion-bridge cycles generating complex subchromosomal amplification[31].

ALL subtypes are driven by different biological pathways

Of the 266 known or putative driver genes affected by SNVs/indels/focal deletions (Supplementary Datasets 1–2), 214 (80%) were altered in both B- and T-ALL (Supplementary tables 11–12). *CDKN2A* alterations (30.7% of B-ALL, 70.3% of T-ALL, Fig. 3a) were associated with high-risk disease (Supplementary Dataset 3 and Supplementary table 13). 93 patients had focal *CDKN2A* deletions not involving *CDKN2B*, whereas *CDKN2B* deletions not involving *CDKN2A* were rare, and deleterious sequence variants were only observed in *CDKN2A* (Supplementary Dataset 1), supporting a pathogenic role for inactivation of INK4A/ARF, but not INK4B in ALL. We also observed key lineage differences, with 49 putative driver genes specific to B-ALL, including multiple distinct histone cluster deletions on 6p22, *ADD3*, *IDH1* and *SLX4IP* (Fig. 3a, Extended data fig. 7a–c and Supplementary table 6). Three genes were specific to T-ALL (*MYCN*, 1.8%; *RPL10*, 5.2% and *FBXO28*, 0.8%; Fig. 3b).

The histone deletions (and occasionally frameshifts) involved a cluster of 32 histone genes (H1, H2A, H2B, H3, H4)[32–35] at 6p22.2 (7.6% of B-ALL samples, most commonly in iAMP21, near haploid, Ph-like, PAX5 P80R, and *ETV6-RUNX1* subtypes) and 21 histone genes at 6p21.1 (2.6% of B-ALL samples) that were frequently heterozygous deletions of a subset of genes in each cluster (Extended data fig. 7a–c), suggesting that loss of all histone genes in each of the regions is deleterious. The burden of SVs was higher in 6p22 histone-altered ALL samples in multiple subtypes (Extended data fig. 7d), consistent with the requirement of histones in DNA damage responses[36,37], and supporting a role in the genesis of iAMP21 ALL (Extended data fig. 7a) where repeated cycles of SV generation occur on chromosome 21[38].

SNVs/indels and CNAs were integrated to identify disrupted biological pathways (Fig. 3c–h and Supplementary table 14). Alterations of transcription factors (other than those regulating B-cell development) and epigenetic regulators were common in both B- and T-ALL (36% vs 50%, *P*=5.58x10^{-7} by two-sided Fisher's exact test and 31% vs 30%, *P*=0.71, respectively; Fig. 3e, h). Pathways enriched in B-ALL included Ras signaling (36% vs 15%, *P*=1.49 x 10^{-17})[39] and B-cell transcription factors (41% vs 5%, *P*=1.26 x 10^{-49})[40], and T-ALL was enriched for alterations in the NOTCH pathway (1% vs 71%, *P*=8.18x10^{-207})[41], cell cycle regulation (predominantly *CDKN2A*, 38% vs 74%, *P*=2.06x10^{-37})[42], JAK-STAT signaling (10% vs 20%, *P*=3.40x10^{-7})[17] and PI3K signaling (3% vs 27%, *P*=1.71x10^{-44}; Fig. 3c–h)[43]. Alterations of the transcription factor genes *IKZF1*, *PAX5* and *ETV6* were common in B-ALL (17%, 23% and 17%, respectively), whereas alterations of *LEF1*, *WT1* and *BCL11B* were almost exclusively present in T-ALL (14%, 10% and 11%, respectively). Alterations were commonly subtype-associated (Supplementary Datasets 4–5 and Supplementary table 12). *CREBBP* alterations were enriched in near haploid (33%) and hyperdiploid B-ALL (15%), whilst alterations of *SETD2* were the highest in PAX5 P80R (23%, Fig. 3a). *SMARCA4* alterations were common in *TLX3* T-ALL subtype (14%). *DUX4*-rearranged ALL had the highest prevalence of epigenetic pathway alterations (66%), dominated by *KMT2D*, *TBL1XR1* and *SETD2* (Fig. 3h).

Hyperdiploid and near haploid ALL showed striking similarity of gene expression (Extended data fig. 2b) and mutations, with frequent epigenetic pathway alterations driven by *CREBBP* (Fig. 3h) and high frequency of Ras pathway alterations (60% and 88%), driven by *NRAS*, *KRAS* and *PTPN11* mutations in hyperdiploid[39] and *NF1* deletion in near haploid ALL[44] (Fig. 3d). The similar expression profiles may have been due to (a) increased relative dosage of chromosomes 10, 14, 18, and 21, as hyperdiploid samples frequently gained these chromosomes, while near haploid often lost all chromosomes except these (Extended data fig. 2b, right); and/or (b) similar cells of origin or developmental stages, consistent with the subtypes being diagnosed at similar ages (median 4.3 years for hyperdiploid and 5.0 years for near haploid; Extended data fig. 2d). Low hypodiploid ALL exhibited common biallelic alteration of *TP53* due to mutation and aneuploidy (85%; somatic 41%, germline 44%), and alteration of *RB1* (30%) and *IKZF2* (25%)[44]. *ETV6-RUNX1*-like ALL[7] harbored non-*ETV6-RUNX1* rearrangements involving *ETV6* (49%), *IKZF1* (14%), *TCF3* (8%), *CRLF2* (5%) and *ERG* (3%; Supplementary table 5). Forty percent (6 of 15) of *ETV6-RUNX1*-like cases lacked rearrangement of a putative driver but most harbored somatic deletions of transcription factors (e.g. *ETV6* (n=2), *IKZF1* (n=1), *PAX5* (n=3)). We identified a similar prevalence of B-cell transcription factor alterations in *ETV6-RUNX1* (46%) vs. *ETV6-RUNX1*-like (47%) subtypes, with a higher frequency of *BTLA-CD200* deletions in *ETV6-RUNX1* (13% vs 0%), while *IKZF1* alterations were more common in *ETV6-RUNX1*-like (2% vs 27%; Fig. 3a). *TBL1XR1* alteration was exclusively identified in *ETV6-RUNX1* (14% vs 0%), whilst deletion of *ARPP21* was enriched in *ETV6-RUNX1*-like (0% vs 27%). Thus, it is interesting that two subtypes with a similar gene signature harbor different driving and secondary alterations also with different clinical outcomes (Extended data fig. 2c). Distinct clusters of Ph+ B-ALL cases were observed by tSNE (Ph1, Ph2 and Ph3; Extended data fig. 2b) with variable secondary genomic alterations: *IKZF1* common in Ph1/Ph2 (76% vs. 88% vs. 13%, respectively), but *PAX5* more common in Ph1 (48% vs. 13% vs. 13%), and aneuploidy most common in Ph3 (0% vs. 8% vs. 45%).

Co-mutation and mutual exclusivity analysis within each ALL subtype (Supplementary Dataset 6 and Supplementary table 15) revealed significant co-occurrence ($P < 0.05$, $Q < 0.05$) of *JAK1* and *JAK3* alterations in *HOXA* T-ALL; of *PHF6* with *DNM2*, *EZH2*, and *JAK1* in *HOXA* T-ALL; of *PAX5* and *IKZF1* alterations in Ph^+ B-ALL; and of chromosome 9p and 20q deletions in Ph-like B-ALL (also associated with ROS-related mutational signature 18, Extended data fig. 5e). Significant mutual exclusivity was observed between *FLT3* and Ras alterations (*NRAS* or *KRAS*) in hyperdiploid B-ALL; between *CDKN2A* and *SUZ12* in *TLX3* T-ALL and between *IKZF1* alterations observed in Ph1 and Ph2 and whole-chromosome gains observed in Ph3 B-ALL.

Driver mutation clonality

In B-ALL, the cancer cell fractions (percent of tumor cells bearing mutations, or CCFs)[45] of lineage-related driver alterations (*ETV6*, *IKZF1*, and *PAX5*) were high, indicating early occurrence, whereas kinase signaling point mutations (*KRAS*, *NRAS*, *JAK1*, *JAK2*, *FLT3*, etc.) were usually subclonal, suggesting later evolutionary occurrence (Fig. 4a, Extended data fig. 8a, and Supplementary table 16). To validate this, we performed simultaneous single-cell DNA sequencing and cell-surface protein expression analysis of three B-ALL patients each having one high-CCF lineage-related mutation (in *IKZF1* or *PAX5*) plus multiple lower-CCF kinase signaling mutations. This confirmed that lineage-related mutations occurred early as they were present in all leukemia cells, while kinase-related mutations appeared later and independently in multiple clones by convergent evolution (Fig. 4b–d). Kinase mutations were often mutually exclusive indicating their presence in different clones (e.g. FLT3 N676K and FLT3 D835E in a hyperdiploid B-ALL sample, Fig. 4b). In one patient, a late-appearing clone bearing PTPN11 D61V had a lower cell-surface protein level of the hematopoietic stem cell marker CD34 (Fig. 4d), suggesting differing hematopoietic differentiation between clones. In two patients, lineage and kinase-related mutations co-occurred in most cells and their order of occurrence could not be resolved (Extended data fig. 8c).

By contrast to B-ALL, in T-ALL certain kinase-related alterations had high CCFs, including *JAK3* and *NRAS* (median CCF >80%, Fig. 4a, Extended data fig. 8b). Further, *JAK1* and *JAK3* mutations co-occurred in the same clone in one *HOXA* T-ALL patient (Extended data fig. 8d), indicating these genes' mutational co-occurrence in this subtype (Supplementary Dataset 6) is not due to convergent evolution in different clones.

Protein modification, RNA machinery and cohesin alterations

Among the 376 putative driver genes, 157 were altered (by coding SNV/indel or focal deletions) in <2% of B-ALL, while 119 were altered in <2% of T-ALL, but collectively, were altered in 54.7% of B-ALL (157 genes) and 51.2% of T-ALL (119 genes). Seventy genes altered in <2% of all samples had not been previously reported in ALL, including 43 genes previously reported in non-ALL tumors and 27 genes not reported as drivers in any malignancy (blue text in Fig. 5 and Extended data fig. 9–10; Supplementary table

6; Supplementary Dataset 1). Of these, predicted loss-of-function or activating alterations in several genes regulating SUMOylation and ubiquitination, and their binding partners (termed protein modification), were present in 9% of B-ALL and 4% of T-ALL (Fig. 5b). Most notable were alterations disrupting UBA2 and SAE1, both of which form a heterodimeric complex essential for SUMOylation[46], in *ETV6-RUNX1* ALL. Alterations affecting ubiquitination included focal deletions of *UHRF1* and sequence mutations in *USP1* (Fig. 5b). Collectively, disruption of genes involved in RNA machinery accounted for 15% of B-ALL and 11% of T-ALL, with enrichment in Ph+, Ph-like and iAMP21 B-ALL subtypes (driven by deletions of *BTG1*) and in *NKX2-1*-rearranged T-ALL driven by *DDX3X*, encoding a member of the DEAD-box helicases (Extended data fig. 9c). Alterations in the cohesin complex were present in 7% of B-ALL and 11% of T-ALL, with the highest frequency observed in the *TLX3* subtype driven by alterations of *CTCF* (Extended data fig. 9d). Genes involved in cytoskeletal assembly were almost exclusively altered in B-ALL (8%) and were largely driven by focal deletions in *ADD3* and the filamin family member, *FLNB*, in Ph+ and Ph-like ALL (Extended data fig. 10a). We also observed somatic alterations in various non-coding RNA genes, including focal deletions of *LINC00649*, *LINC02227*, and *MIR181A1HG*, particularly in Ph^+ and Ph-like subtypes (Fig. 5c). *MIR181A1HG* is expressed in hematopoietic stem/progenitor cells with decreasing expression during myeloid differentiation[47], suggesting that deletions may affect lineage fate. Thus, as observed in solid tumors[48], a "long tail" of somatically altered genes converging on common pathways is a hallmark of ALL.

Genomic determinants of outcome

The overall survival (OS) for each ALL subtype is shown in Extended data fig. 2c and 3c. The prognostic contribution of secondary genomic alterations was assessed by univariate analysis for OS, event-free survival (EFS), and the presence/absence of minimal residual disease (MRD) at the end of induction therapy in B-ALL and T-ALL, and within each ALL subtype (Fig. 6a–b, Supplementary Datasets 7–8 and Supplementary tables 17–19). Alterations significantly associated with OS or EFS within specific subtypes by univariate analysis ($P \leq 0.05$ by log-rank test, shown by red and blue cells in Fig. 6a, b) were further analyzed by multivariate Cox proportional-hazards analysis incorporating age, WBC count, MRD presence/absence, and treatment protocol ($P \leq 0.05$ shown by yellow diamonds in Fig. 6a, b; Supplementary tables 20–21; see Methods). In B-ALL, we confirmed the inferior outcome of *IKZF1*$^{\text{plus}}$ compared to patients with *IKZF1* deletion who did not fulfill the *IKZF1*$^{\text{plus}}$ definition (10-year OS 73.8% vs 80.9%, P=6 x 10^{-11} by log-rank test)[49]. Alterations associated with inferior outcomes in specific B-ALL subtypes included *TBL1XR1* in *ETV6-RUNX1* ALL (5-year OS 89.0% vs. 99.6% in altered vs. non-altered, P=0.004 by multivariate Cox analysis), *SETD2* in hyperdiploid ALL (5-year EFS 46.9% vs. 94.9%, P=7x10^{-6}), and *CDKN2A* in *TCF3-PBX1* ALL (5-year EFS 63.6% vs. 92.7%, P=0.03) (Fig. 6c–e). In T-ALL, alterations of *PHF6* were associated with poor OS in the *TAL1* subtype (60.0% vs. 92.6%, P=2.3 x 10^{-4}) (Fig. 6f). Increased age was not the explanation for the poor outcomes associated with these alterations. Indeed, nearly all alterations significantly associated with outcomes by multivariate analysis (yellow diamonds in Fig. 6a, b) were not significantly associated with age, with the exception of *TBL1XR1* alterations (median 4.9 years old at diagnosis vs. 3.8 years for non-altered; P=0.0002 by Wilcoxon rank-sum test) and *UHRF1* alterations (5.4 vs. 4.1 years; *P*=0.04) in *ETV6-RUNX1* B-ALL, though these alterations were still significantly associated with outcomes independent of age by multivariate analysis (Fig. 6a, b; Supplementary tables 20–21).

Subtypes within *DUX4*- and *KMT2A*-rearranged ALL

We identified distinct gene expression clusters for *DUX4*- and *KMT2A*-rearranged subtypes by tSNE analysis, termed *DUX4*-a and *DUX4*-b, and *KMT2A*-a and *KMT2A*-b (Fig. 7a). The *DUX4*-a and -b subgroups had differing mutational landscapes, with *ERG* and *TBL1XR1* alterations enriched in *DUX4*-a and *NRAS*, *IKZF1*, and *KMT2D* enriched in *DUX4*-b (Fig. 7b); the latter subgroup also had worse EFS but not OS by univariate analysis (Fig. 7c; multivariate analysis was not possible). *PAX5* alterations were enriched in *KMT2A*-a compared to *KMT2A*-b (Fig. 7b), though no difference in EFS or OS survival was observed. The *DUX4*-a and *KMT2A*-a subgroups had high expression of *NFATC4*, whilst the reciprocal subtypes *DUX4*-b and *KMT2A*-b showed high expression of *CEBPA* and *FLT3* (Fig. 7d–e and Supplementary tables 22–23). *NFATC4* is expressed in pre-B and immature B cells[50] in mice, whereas *CEBPA* and *FLT3* are co-expressed in common lymphoid progenitors and pre-pro-B cells[51], suggesting a developmental difference between a and b subgroups.

Germline variants in ALL

Forty-seven of 1,703 patients with germline WES (2.8%) had pathogenic or likely pathogenic germline variants known to promote cancer development, including in *TP53* (n=9, including 8 low hypodiploid B-ALL cases), *ETV6* (n=9, including 5 in hyperdiploid and 2 in *ETV6-RUNX1*-like B-ALL), *BRCA2* (n=8) and *BRCA1* (n=6) spread across multiple B- and T-ALL subtypes, and *PTPN11* (n=3). An additional 5 patients had germline variants without known germline cancer association, but which are somatically altered in ALL, including two *HDAC7* variants (Supplementary table 24).

Discussion

This study highlights the complex genomic relationship between molecular subtypes and their secondary alterations that drive leukemogenesis and outcome in childhood ALL. Unexpectedly, most pediatric ALL subtypes had a similar number of putative driver gene alterations as adult cancers (4-5 per sample)[52], perhaps due to accelerated rates of focal deletions which are promoted by RAG1/2-mediated recombination in lymphocyte progenitor cells[53,54]. However, several B-ALL subtypes had only 2-3 putative driver alterations per sample (including *KMT2A*-rearranged, *TCF3-PBX1*, and aneuploid subtypes), perhaps due to earlier age of onset or a lower requirement for secondary alterations of putative driver genes.

Conflicting studies have proposed that acquisition of hyperdiploidy is a single early event[55,56], while others suggest sequential and ongoing acquisition of chromosome gains[57]. Our results indicate that the majority of hyperdiploid ALL originates from a “big bang” of simultaneous or closely temporally juxtaposed chromosomal gains in a single aberrant mitosis or in multiple cell divisions within a short time frame. Chromosomal gains are likely commonly acquired in utero followed by mutational evolution, often involving epigenetic regulators and Ras signaling. By contrast, in B-ALL with iAMP21, the characteristic copy gains commonly postdate sequence mutations, consistent with the later age of onset of this subtype. Collectively, these observations support a model for the development of the majority of subtypes of childhood B-ALL in which aneuploidy or oncogenic translocations early in life are the initiating leukemogenic events. These are followed by focal deletions, including RAG-mediated deletions that are a by-product of lymphoid expansion that accompanies maturation of the immune response in early childhood. Such deletions and sequence mutations are selected for if they further promote (pre-)leukemic fitness.

It is unclear whether UV-associated signature 7, which we detected in a subset of aneuploid ALL samples, is caused by UV itself or a biochemical mimic. However, we suspect signature 7 is UV-induced in ALL. First, we previously observed signature 7 primarily ALL patients of European ancestry but not those of African descent[24], and in this study we likewise found a trend towards signature 7 enrichment in non-African ancestry patients (34.3% signature 7-positive among hyperdiploid, iAMP21, and near haploid B-ALL) compared to African ancestry patients (9.1%; $P = 0.10$ by Fisher's exact test). Second, the highest incidence of ALL occurs in patients of European ancestry, with a lower incidence in patients of African descent[24]. Third, extensive chemical profiling has not revealed biochemical causes of signature 7 outside of UV[58]. Fourth, the abundance of signature 7 does not increase with age, consistent with an intermittent environmental exposure such as UV. Finally, in hyperdiploid B-ALL signature 7 is only present on 1/3 alleles in 3-copy regions, consistent with UV-induced mutations appearing after copy gains, which likely occur in utero[30] where UV exposure is unlikely (whereas signature 7 mutations on 2/3 alleles would indicate prenatal exposure). UV light is capable of penetrating skin sufficiently to affect dermal blood[59], and since hyperdiploidy is often detectable at birth in preleukemic blasts from peripheral blood[30,60], UV light may affect these pre-malignant blasts in circulation in dermal skin and thus promote mutagenesis leading to frank ALL. Lymphocytes in general are susceptible to UV-induced mutagenesis as signature 7 has been detected in cutaneous T-cell lymphomas[61].

The late appearance of kinase signaling point mutations involved in the Ras and JAK-STAT pathway in our B-ALL cohort and prior studies showing the unpredictable nature of their convergence and extinction at relapse[62] cautions against therapeutic targeting of these alterations. However, in T-ALL certain kinase alterations, including *JAK3* and *NRAS*, appear to be early events and may merit pharmacological targeting. The *KMT2A*-b subgroup may be preferentially susceptible to FLT3 inhibitors, recently used in clinical trials of *KMT2A*-rearranged B-ALL[63], based on higher *FLT3* expression.

ETV6-RUNX1 and hyperdiploid ALL are the most common subtypes with extremely good outcomes, yet a subset of these patients relapse, the reasons for which are still unclear, in part as many prior comprehensive sequencing studies have focused on high risk subtypes. However, defining the drivers of treatment failure in standard-risk patients is crucial as approximately half of all relapses occur in children initially diagnosed with standard-risk disease. A notable finding of this study is that specific secondary mutations, particularly in epigenetic regulators (*TBL1XR*1 in *ETV6-RUNX1* and *SETD2* in hyperdiploid ALL), may improve risk stratification. Patients lacking these mutations had OS rates over 99%, while those with mutations had significantly inferior survival. We did not confirm the prognostic impact of the *NOTCH1*/*FBXW7*/*RAS*/*PTEN* classifier in all T-ALL cases[64] but show subtype specificity, with *NOTCH1* mutations having a favorable outcome in *TLX3* and *PTEN* deletions predicting poor outcome in the *TAL1* subtype, indicating that future risk stratification classifiers should consider both genetic alterations and molecular subtypes.

Overall, we identified 376 putative driver genes in ALL. Although the list of individually altered putative drivers is long, and the genes involved vary between patients and subtypes, these drivers converge on key pathways whose alteration is often essential to initiate and facilitate transformation: perturbation of lymphoid maturation, transcriptional deregulation, cell cycle regulation, multiple types of chromatin modification, and kinase signaling. Seventy of these have not been identified in ALL, and each gene was altered in less than 2% of patients. Collectively, infrequently altered genes are present in approximately half of ALL patients and converge on several key biological pathways not previously associated with ALL, including protein modification, RNA machinery and the cohesin complex, which were collectively altered in 8, 14, and 8% of cases respectively. Thus, multiple genomic scenarios contribute to the development of ALL. Indeed, the enrichment of genes and the identification of unique gene combinations that exists across ALL subtypes highlights the wide diversity in disease mechanisms across subtypes and will guide the development of experimental models that faithfully recapitulate human disease.

Methods

Patients and clinical specimens

The study complies with all ethical regulations and was approved by the Institutional Review Boards of St. Jude Children's Research Hospital and the Children's Oncology Group. Written informed consent was obtained from the patient, parents or guardians. Subjects were not compensated for participation. We studied 2754 children, adolescents and young adults (AYA) with newly diagnosed B-ALL (n=2288) or T-ALL (n=466) enrolled-on St. Jude Children's Research Hospital (St. Jude, n=899) and Children's Oncology Group (COG, n=1855) protocols, including St. Jude Total XV[65] (ClinicalTrials.gov Identifier NCT00137111), St. Jude Total XVI[66] (NCT00549848), COG P9906 high-risk B-ALL study[67] (NCT00005603), COG AALL0232 NCI high-risk B-ALL study[68] (NCT00075725), COG AALL1131 high-risk B-ALL study[69] (NCT02883049), COG AALL0331 standard-risk B-ALL study[70] (NCT00103285), COG AALL0932 standard-risk B-ALL study[71] (NCT01190930), and COG AALL0434 T-ALL study[72] (NCT00408005) (Extended data fig. 1, Supplementary table 1). Matched normal control DNA was derived from remission blood or bone marrow with negative or low (<5%) measurable residual disease by flow cytometry, or by purifying non-tumor cells by fluorescence-activated cell sorting (Supplementary fig. 1).

No statistical methods were used to predetermine sample size. The experiments were not randomized and investigators were not blinded to allocation during experiments and outcome assessment. Genomic analysis was performed on distinct samples and the same sample was not measured repeatedly.

Transcriptome sequencing and statistical analyses

Details of transcriptome sequencing, gene expression evaluation from RNA-seq, B- and T-ALL subtyping and statistical analyses are provided in the Supplementary Note.

Somatic copy number alteration identification

For Illumina-based WGS data, we performed alignment with BWA version 0.5.9 (hg19), and identified somatic CNAs using CONSERTING version 1.0. For CGI (Complete Genomics Inc.)-based WGS data, we used CNA data from our previously published analysis which used an adaptation of CONSERTING to call CNAs[24]. Focal deletions in known or putative driver genes were identified as those that were shorter than 5 megabases (Mb) in length, and (in protein-coding genes) affected any exon in the gene of interest which contained a coding region or (in non-coding genes) affected any exon in the gene. However, for *CDKN2A*, *PAX5*, and *IKZF1*, focal deletions of 20 Mb or less were also considered alterations due to their well-established driver status. A $\log_2$ fold change of −0.15 or less was required to consider a gene focally deleted, except for in near haploid and low hypodiploid subtype samples, where a threshold of −1.0 or less (essentially homozygous deletions) was required. Focal deletions were only noted in genes considered likely to be tumor suppressors based on known function, preponderance of focal deletions, or preponderance of frameshift and nonsense mutations (Supplementary table 6).

Somatic structural variant identification

Somatic SVs were identified from Illumina-based WGS data aligned to hg19 using BWA version 0.5.9. SVs were called using four callers: CREST version 1.0[73], SvABA version 1.1.3[74], Manta version 1.6.0[75], and Delly version 0.8.2.[76] SVs detected by two or more of these four callers were included in the final call set similar to analysis done in the Pan-Cancer Analysis of Whole Genomes (PCAWG) structural variant study[77]. SVs were considered matching between two callers if both breakpoints were within 30 bases and had the same structural orientation. CREST calls were manually reviewed in the Bambino-based BamViewer to exclude spurious variants[78], and selected likely driver alterations detected only by CREST were rescued and included in the final call set even if not detected by another caller, including rearrangements expected based on RNA-Seq-based transcriptional clustering or fusion detection, and deletions with breakpoints matching CNAs. SVs for CGI-based WGS data were obtained from our previous study in which SVs were identified using the CGI Cancer Sequencing service pipeline (version 2) and filtered to remove germline SVs[24].

Somatic SNV and indel identification

Somatic SNVs and indels were identified from Illumina-based WGS and WES data with Bambino version 1.6 after alignment with BWA (hg19). Exonic variants were manually viewed in BamViewer[78] and those with weak evidence upon visual inspection were removed from consideration. For previously published Illumina samples, the Bambino SNV and indel calls were used from the original study (see Supplementary tables 3–4). For CGI-based WGS data, SNVs and indels were used from our previous study, where we downloaded TARGET variant calls and used filters to remove likely artefactual variants[24]. SNVs and indels were annotated using VEP version 95.2[79]. For 318 samples sequenced with both Illumina-based WGS and WES, SNVs detected in only one of these two platforms were subjected to a detailed check for mutant reads in the undetected platform using a custom script. After performing this analysis there was 95% concordance (overlapping variants / total variants) between the two platforms when analyzing somatic SNVs with at least 10 reads of coverage in both platforms. In samples with both WGS and WES, variants called with either platform (either WGS or WES) were included analysis.

Given 50x coverage (the median for WGS), there was 98.6% probability of detecting a variant with at least 3 mutant reads (the minimum required for *de novo* variant calling) given a true VAF of 15%. The probability decreased to 88.8% given a VAF of 10%, or 45.9% given a VAF of 5%. Given 72x coverage (the median for WES), these probabilities were 99.9% (for 15% VAF), 97.9% (10% VAF), and 70.5% (5% VAF).

Germline SNV and indel identification

Germline SNVs and indels were detected from WES data using Bambino version 1.6 after alignment with BWA (hg19). The impact of the variants on protein coding genes was annotated with ANNOVAR (version 2014-11-12)[80] with multiple databases. The following criteria were applied to keep the potential pathogenic (P) and likely pathogenic (LP) variants: (1) germline SNVs had mutant variant allele fraction (VAF) of at least 0.2 to be considered; (2) variants had MAFs (minor allele frequencies) less than 0.001 in 1000 Genomes, EVS, and ExAC population allele frequency databases; (3) frameshift and splice indels were considered; (4) nonsense and splice SNVs were also considered; and (5) missense variants with a REVEL[81] score >0.5 were considered. Variants meeting these criteria were then analyzed following American College of Medical Genetics (ACMG) guidelines. Variants meeting ACMG guidelines for pathogenicity (P or LP) were considered germline predisposition variants (Supplementary table 24), and corroborated with ClinVar when possible.

SNV burden quantification

The SNV burden, as shown in Fig. 1, was quantified for all samples sequenced by WGS or WES. For samples sequenced by both WGS and WES, only the WGS SNVs were analyzed. All SNVs found in protein-coding genomic positions, whether synonymous (silent) or non-synonymous (including missense, nonsense, etc.) were analyzed. SNVs found in regions of genes not coding for proteins (such as introns, UTRs, etc.) were excluded. The total calculated length of protein-coding regions of the genome was 34,246,114 base pairs, based on the UCSC refGene.txt (hg19) transcript annotation file. The number of SNVs (which were found in these protein-coding regions) in each sample was divided by this number and multiplied by 10^6 to obtain the number of SNVs per Mb in the sample.

Identification of significantly mutated or altered genes

To identify significant somatic mutated or altered genes, we used MutSigCV version 1.4 (SNVs and indels as input)[20], GRIN (SNVs, indels, and CNA data; GRIN is not versioned currently)[21], GISTIC version 2.0 (CNA data)[22], SV outliers (SV input; genes where 5 or more samples had an SV breakpoint within the gene were checked for recurrent focal deletions), and MedalCeremony (version 1.0)[23]. MutSigCV was also run on B-ALL alone and T-ALL alone, in addition to the entire cohort. Genes with $P < 0.05$ and $Q < 0.25$ by MutSigCV or GRIN were considered putative driver genes. Manual inspection of SNV/indel mutations across each protein thus identified, using ProteinPaint[82], was used to confirm significance, and genes were manually removed from consideration as putative drivers if their profile was inconsistent with likely oncogenic or tumor suppressor function (e.g. a profile including only diffuse, non-hotspot missense mutations). A few genes with recurrent hotspot SNVs/indels were considered putative driver alterations despite lack of statistical significance. Putative driver genes were considered to be not previously reported in cancer if not part of the Sanger Cancer Gene Census[25], not reported as significantly mutated in our previous pan-cancer study[24], and not reported as mutated in cancer based on our search of the literature. Genes reported in a non-ALL cancer type, but not in ALL, in the Sanger Cancer Gene Census, our previous pan-cancer study, or the literature were considered newly reported in ALL in this study.

Driver alteration identification and driver burden quantification

The driver alteration burden in Fig. 1 was calculated as follows, and only samples with SNV/indel and copy number characterisation (WGS or WES plus SNP copy array) were analyzed. Known driver genes, or putative driver genes identified from significantly mutated gene analysis (see Supplementary table 6 for full list), were considered altered in a sample if mutated in a way consistent with their oncogene or tumor suppressor status. Oncogenes required variants to be coding alterations including missense, splice site, and in-frame indels. Tumor suppressor genes allowed all of these variant types plus nonsense and frameshift variants, and focal deletions of 5 Mb or less. (These are also the criteria used to determine whether driver or putative driver genes were considered altered in other analyses in the study.) If the gene was altered more than once in the sample (such as biallelic alteration) it was only counted once in the driver gene burden. Canonical and likely driver fusions, detected by WGS, RNA-seq, or clinical methods, were counted as a single driver event. In ALL samples where a single driver rearrangement was expected (based on the subtype) but not detected due to lack of a platform able to detect it (for example, a DUX4 subtype sample with high *DUX4* expression but no *IGH-DUX4* detected due to lack of WGS), one driver rearrangement event was assumed in addition to the driver SNVs/indels or focal deletions actually detected.

In addition to driver SNVs/indels, focal deletions, and known fusions/rearrangements, selected genes were characterized for special variant types, including in *FLT3* (enhancer-activating focal deletions similar to those reported previously[83], termed “regulatory” in figures), and in *PAG1* and *TBL1XR1* (focal promoter deletions, grouped with “focal deletions” in figures). The above-mentioned *FLT3* alterations were associated with increased *FLT3* expression, while the above-mentioned *PAG1* and *TBL1XR1* alterations were associated with decreased expression, leading to these alterations being considered driver alterations.

Pathway analysis

Genes were manually assigned to various signaling and functional pathways as described in Supplementary table 14. If at least one gene in the pathway was somatically altered (with an alteration matching the gene's putative oncogene or tumor suppressor status, where missense and splice-site SNVs and in-frame indels were considered drivers for oncogenes, while for tumor suppressors missense, splice-site, in-frame indels, nonsense, frameshift, and focal deletions (of 5 Mb or less) were considered driver alterations as per Supplementary table 6; fusions and rearrangements were not considered), the pathway was considered altered in that sample. Overall survival, event-free survival, and subtype enrichment for each pathway were then compared as done for individual genes, comparing pathway-positive vs. pathway-negative samples. The transcription and epigenetic pathways excluded genes mutated in less than 2% of B-ALL and in less than 2% of T-ALL due to the large number of genes included in these pathways.

Mutational signature analysis

Genome-wide SNVs from WGS samples were identified as described above; variants in repetitive genomic regions were excluded. Each variant's trinucleotide context was determined using an in-house script (hg19 reference genome) to obtain the 96-channel profile for each sample[84]. The presence and strength of the COSMIC version 3.0 mutational signatures in each sample was determined using MATLAB-based SigProfilerSingleSample (version 1.3)[27] using the COSMIC signature set included in that software version and default parameters, plus previously unreported signatures we recently discovered[85]. COSMIC signature 7 levels noted in the text and figures refer to the sum of signatures 7a, 7b, 7c, and 7d. African vs. non-African descent was determined for hyperdiploid, iAMP21, and near haploid B-ALL samples with Illumina WGS based on (when available) self-reported race, or (when unavailable) principal component analysis clustering of germline SNPs (detected by WGS) informed by the cases with known self-reported race.

Timing of copy number alterations in aneuploid subtypes

WGS samples belong to hyperdiploid and iAMP21 B-ALL subtypes were analyzed. Integer copy number states of each CONSERTING-identified copy number segment was first performed in order to identify SNVs in 3-copy regions. Copy number data were manually centered at the diploid center peak if needed, based on allelic imbalance and copy number information. 1- and 3-copy states were then identified using allelic imbalance and copy number information, and to correct for tumor purity, the linear (non-log) copy number data were multiplied around the 2-axis (diploid state) to align apparent 1- and 3-copy states in impure samples with actual 1- and 3-copy numerical values. SNVs in 3-copy regions were those with a linear (not log) copy number of 2.5 to 3.49.

For comparing the UV signature between variants on 1/3 or 2/3 copies, mutations were considered to be on 1/3 copies if below VAF 0.5 (adjusted for tumor purity) or 2/3 copies if above 0.5. Variants were pooled within all hyperdiploid or all iAMP21 samples, followed by mutational signature analysis to determine the presence or absence of the UV signature on 1/3 or 2/3 copies.

For determining whether hyperdiploid copy gains occurred synchronously or asynchronously, each 3-copy chromosome with at least 20 SNVs was analyzed using WGS. Only samples with two or more such chromosomes were analyzed. The somatic SNV VAFs, adjusted for tumor purity, were analyzed for each 3-copy chromosome, and samples where all chromosomes had a similar ratio of 1/3 (VAF 0.33) vs. 2/3 (VAF 0.67) SNVs in 3-copy regions were considered to have synchronous copy gains. Samples where the ratio was different for different chromosomes were considered to have asynchronous copy gains.

Cancer cell fraction calculation

Cancer cell fractions (CCFs) were determined for driver or putative driver gene SNVs and indels in 2-copy regions for most subtypes. The CCF for these was as follows, where p indicates tumor purity:

$$CCF = \frac{2^{*}VAF}{p} \tag{1}$$

In near haploid and low hypodiploid samples, variants in 1-copy regions were used. The proportion of tumor reads (t) in the sample was defined as (only for 1-copy region variants):

$$t = \frac{p}{(p + 2(1 - p))} \tag{2}$$

The 2(1-p) indicates the normal cell (diploid) read contribution. The CCF was then defined as (only for 1-copy region variants):

$$CCF = \frac{VAF}{t} \tag{3}$$

Single-cell DNA sequencing and protein analysis

Single-cell amplicon-based DNA and protein sequencing was performed on six ALL samples using the Tapestri (version 2) platform (MissionBio), and the ALL amplicon panel, which analyzes common mutations in 305 genomic regions within 112 ALL driver genes[86]. Ten TotalSeq oligo-conjugated antibodies from Biolegend were used for cell-surface protein analysis: D0048 anti-human CD45, D0054 anti-human CD34, D0066 anti-human CD7, D0063 anti-human CD45RA, D0062 anti-human CD10, D0050 anti-human CD19, D0389 anti-human CD38, D0052 anti-human CD33, D0034 anti-human CD3 and D0138 anti-human CD5. Cryopreserved mononuclear cells were thawed, deprived of dead cells by using the Dead Cell Removal Kit (Miltenyi Biotech, #130-090-101), resuspended in Cell Staining Buffer (BioLegend, 420201) (CSB), counted by a Countess II Automated Cell Counter (Thermo Fisher) and diluted to have 25,000 cells/μL using CSB in a minimum volume of 40 μL. Cell suspension was processed according to the Tapestri Single-Cell DNA + Protein Sequencing User Guide. Briefly, cells were incubated with TruStain FcX and Blocking Buffer (Mission Bio) for 15 minutes (min) on ice. The pool of 10 oligo-conjugated antibodies described above was then added and incubated for 30 min on ice. Cells were then washed multiple times with pre-chilled CSB, counted to have a cell suspension of 3,000 – 4,000 cells/μL and loaded on a Tapestri microfluidics cartridge. Single cells were encapsulated with Lysis Buffer and Protease (Mission Bio) to create a cell emulsion and barcoded. DNA PCR products were then isolated from individual droplets, purified with Ampure XP beads (Beckam Coulter) and used for library generation. The supernatant from the Ampure XP bead incubation above contained the protein PCR products and it was incubated with biotin oligo (5 μM, Mission Bio) at 96 °C for 5 min followed by incubation on ice for 5 min. Protein PCR products were then purified using Steptavidin beads (Mission Bio) and used for library preparation. All libraries, both DNA and protein, were purified by Ampure XP beads, quantified and pooled for sequencing on an Illumina NovaSeq.

The resulting fastq files for single-cell DNA and protein libraries were analyzed through the Tapestri pipeline in the Tapestri Portal. This pipeline trims adapter sequences, detects barcodes, aligns reads to the human genome (hg19), assigns sequence reads to cell barcodes, and performs mutation identification using GATK. For each single cell, mutation VAFs were calculated from GATK mutation calls for each expected driver variant which was originally detected by bulk sequencing, plus additional driver variants detected *de novo* from single-cell sequencing. Only cells with at least 10 reads of coverage at all of the expected driver mutation sites were analyzed, and a positive mutation call required at least 2 mutant reads and a VAF of 10% or more. In two patients, important driver variants were missed by GATK but were found in the single-cell DNA sequencing bam files. Therefore, in these patients, the GATK mutation counts were not used, but instead a custom script was used to obtain mutant and total read coverage at each driver mutation site from each single cell's bam file. For single-cell protein analysis, in each cell the percent of protein-associated sequencing reads assigned to each of the 10 proteins was calculated as a measure of that protein's level.

Data availability

Genomic data is publicly available and data accessions for RNA-seq, WES, WGS and SNP are listed for each case in Supplementary table 1. TARGET ALL data may be accessed through the TARGET website at https://ocg.cancer.gov/programs/target/data-matrix. The TARGET BAM and FASTQ sequence files are accessible through the database of genotypes and phenotypes (dbGaP; https://www.ncbi.nlm.nih.gov/projects/gap/cgi-bin/study.cgi?study_id=phs000218.v24.p8) under accession number phs000218 (TARGET) and at NCI's Genomic Data Commons http://gdc.cancer.gov_under project TARGET. The remaining (non-TARGET) data has been deposited in the European Genome Phenome Archive, accessions EGAS00001000447, EGAS00001000654, EGAS00001001923, EGAS00001001952, EGAS00001002217, EGAS00001003266, EGAS00001004810, EGAS00001004998, EGAS00001005084 and EGAS00001005250 and is also accessible through St. Jude Cloud at https://platform.stjude.cloud/data/cohorts?dataset_accession=SJC-DS-1009. All raw sequencing data is available under controlled access for protection of germline information and to ensure appropriate data usage, and approval can be obtained by applying through the dbGaP portal (for TARGET datasets) or by contacting the PCGP steering committee (PCGP_data_request@stjude.org) for non-TARGET (EGA-deposited) datasets. Somatic mutation data can also be explored interactively using ProteinPaint[82] and GenomePaint[87] on St. Jude Cloud at https://viz.stjude.cloud/mullighan-lab/collection/the-genomic-landscape-of-pediatric-acute-lymphoblastic-leukemia~15.

Code availability

This study did not involve the development of custom code.

Extended Data

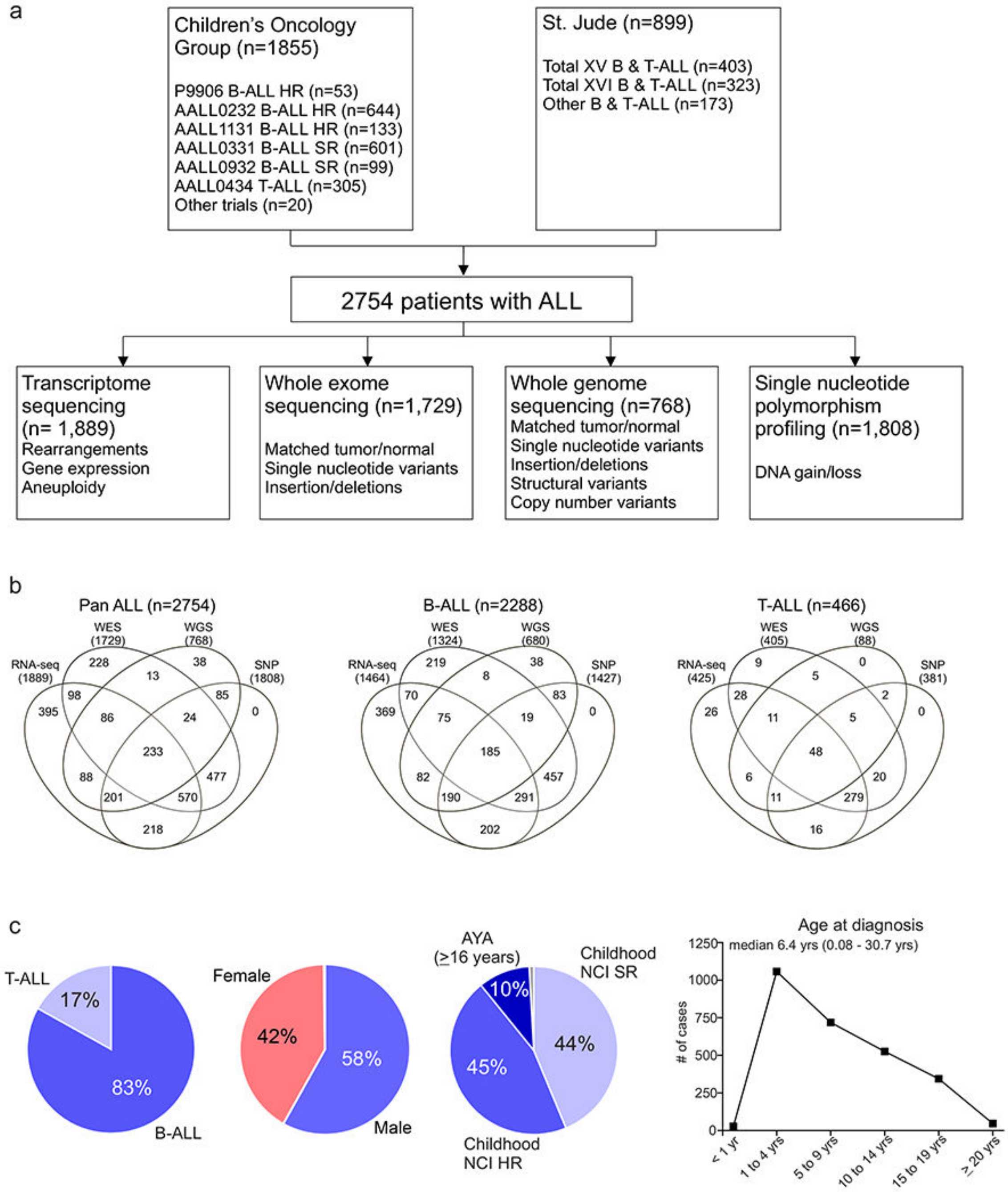

Extended Data Fig. 1. Overview of ALL cohort

(a) Number of acute lymphoblastic leukemia (ALL) patients studied (n=2754), the different modalities of sequencing performed, and the genomic alterations identified by each. (b)

Venn diagram of samples analysed by transcriptome sequencing (RNA-seq), whole exome sequencing (WES), whole genome sequencing (WGS) and single nucleotide polymorphism (SNP) profiling across the whole cohort (Pan ALL; left), in B-ALL only (middle) and in T-ALL only. (c) Distribution of patients according to lineage (left), sex (middle left), NCI standard-risk (SR), age 1 to 9.99 yrs and WBC < 50,000/μl; high-risk (HR), age 10 to 15.9 yrs and/or WBC ≥ 50,000/μl; adolescent and young adult (AYA; middle right) and age at diagnosis (right).

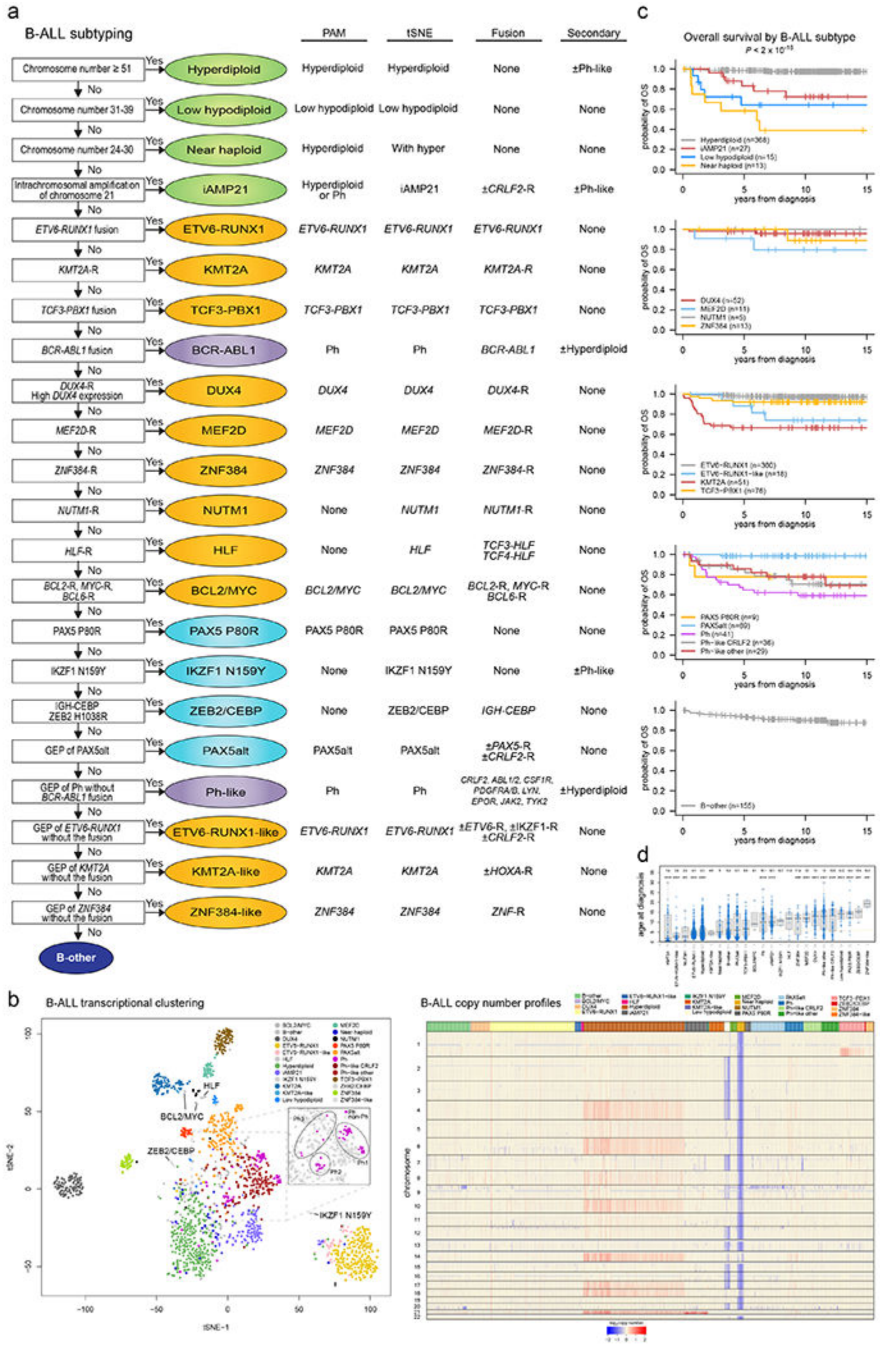

	PAM	tSNE	Fusion	Secondary
Hyperdiploid	Hyperdiploid	Hyperdiploid	None	±Ph-like
Low hypodiploid	Low hypodiploid	Low hypodiploid	None	None
Near haploid	Hyperdiploid	With hyper	None	None
iAMP21	Hyperdiploid or Ph	iAMP21	±CRLF2-R	±Ph-like
ETV6-RUNX1	ETV6-RUNX1	ETV6-RUNX1	ETV6-RUNX1	None
KMT2A	KMT2A	KMT2A	KMT2A-R	None
TCF3-PBX1	TCF3-PBX1	TCF3-PBX1	TCF3-PBX1	None
BCR-ABL1	Ph	Ph	BCR-ABL1	±Hyperdiploid
DUX4	DUX4	DUX4	DUX4-R	None
MEF2D	MEF2D	MEF2D	MEF2D-R	None
ZNF384	ZNF384	ZNF384	ZNF384-R	None
NUTM1	None	NUTM1	NUTM1-R	None
HLF	None	HLF	TCF3-HLF TCF4-HLF	None
BCL2/MYC	BCL2/MYC	BCL2/MYC	BCL2-R, MYC-R BCL6-R	None
PAX5 P80R	PAX5 P80R	PAX5 P80R	None	None
IKZF1 N159Y	None	IKZF1 N159Y	None	±Ph-like
ZEB2/CEBP	None	ZEB2/CEBP	IGH-CEBP	None
PAX5alt	PAX5alt	PAX5alt	±PAX5-R ±CRLF2-R	None
Ph-like	Ph	Ph	CRLF2, ABL1/2, CSF1R, PDGFRA/B, LYN, EPOR, JAK2, TYK2	±Hyperdiploid
ETV6-RUNX1-like	ETV6-RUNX1	ETV6-RUNX1	±ETV6-R, ±IKZF1-R ±CRLF2-R	None
KMT2A-like	KMT2A	KMT2A	±HOXA-R	None
ZNF384-like	ZNF384	ZNF384	ZNF-R	None

Extended Data Fig. 2. Subtype classification of B-ALL

(**a**) Flow chart for B-ALL subtype classification; for detailed description of criteria, see Supplementary Methods. (**b**) Left, tSNE of B-ALL cases with RNA-seq. Right, copy number heatmap of B-ALL samples as determined by WGS or SNP copy array (n=1,630 samples), with subtype indicated by color at top. (**c**) Kaplan-Meier survival curves with overall survival distributions for each B-ALL subtype. Subtypes are separated into five graphs for ease of visualizing the various subtypes. Subtypes with at least 5 samples are shown. *P* value shown is by two-sided log-rank test comparing all subtypes shown in all five graphs. (**d**) Age at diagnosis by B-ALL subtype. Boxplot shows median (thick center line) and interquartile range (box). Whiskers are described in R boxplot documentation (a 1.5*interquartile range rule is used). Text at top shows median age in the subtype. *P* values compare ages from the subtype vs. all other B-ALL samples by Wilcoxon rank-sum test; *P* values ≤ 0.05 are shown. Numbers of patients are shown at bottom, and yellow line indicates median age across B-ALL.

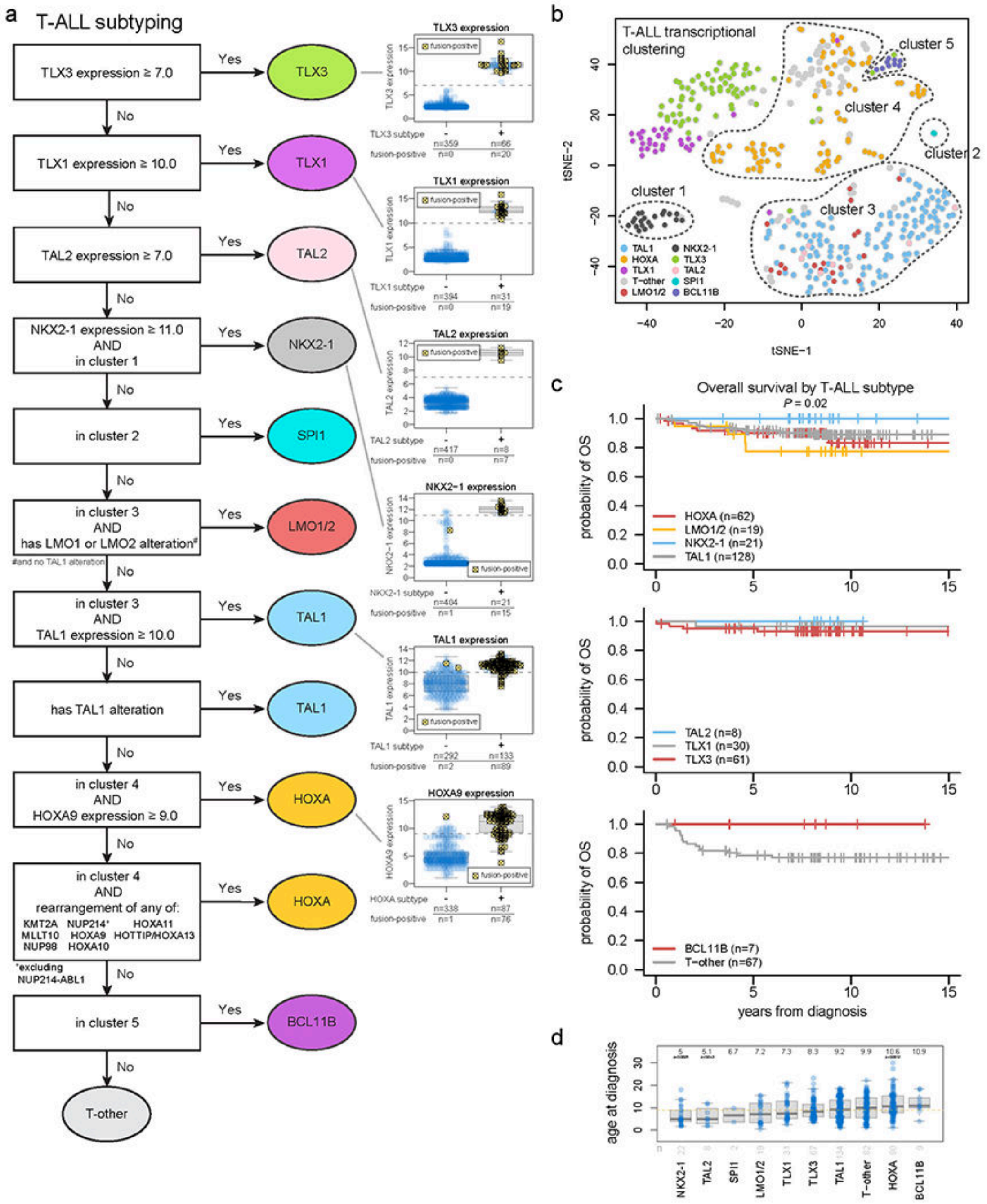

Extended Data Fig. 3. Subtype classification of T-ALL

(**a**) Flow chart for T-ALL subtype classification and inclusion in clusters 1-4 as drawn on the tSNE plot. Classification begins at the top and samples meeting the indicated criteria are assigned to subtypes shown at right. Boxplots to the right show the expression of these genes in samples assigned to the indicated subtype (+) or not assigned (−). Samples bearing a detected fusion or rearrangement defining the subtype are marked with yellow circles with X marks. The gene expression thresholds indicated at left were determined based on the expression levels in fusion-positive samples. Samples where gene expression was above these thresholds but no fusion was detected were assumed to likely have a fusion and were thus assigned to that subtype, since the fusion may have been undetected due to technical issues (e.g. TLX3 enhancer hijacking rearrangements may be hard to detect with RNA-seq since they do not always create fusion transcripts). Boxplots show median (thick center line) and interquartile range (box). Whiskers are described in R boxplot documentation (a 1.5*interquartile range rule is used). (**b**) tSNE of T-ALL cases with RNA-seq. (**c**) Kaplan-Meier survival curves with overall survival distributions for each T-ALL subtype, shown in three graphs for ease of visualization. Subtypes with at least 5 samples are shown. *P* value shown is by two-sided log-rank test comparing all subtypes shown in all graphs. (**d**) Age at diagnosis by T-ALL subtype. Boxplot shows median (thick center line) and interquartile range (box). Whiskers are described in R boxplot documentation (a 1.5*interquartile range rule is used). Text at top shows median age in the subtype. *P* values compare ages from the subtype vs. all other T-ALL samples by two-sided Wilcoxon rank-sum test; *P* values ≤ 0.05 are shown. Numbers of patients are shown at bottom, and yellow line indicates median age across T-ALL.

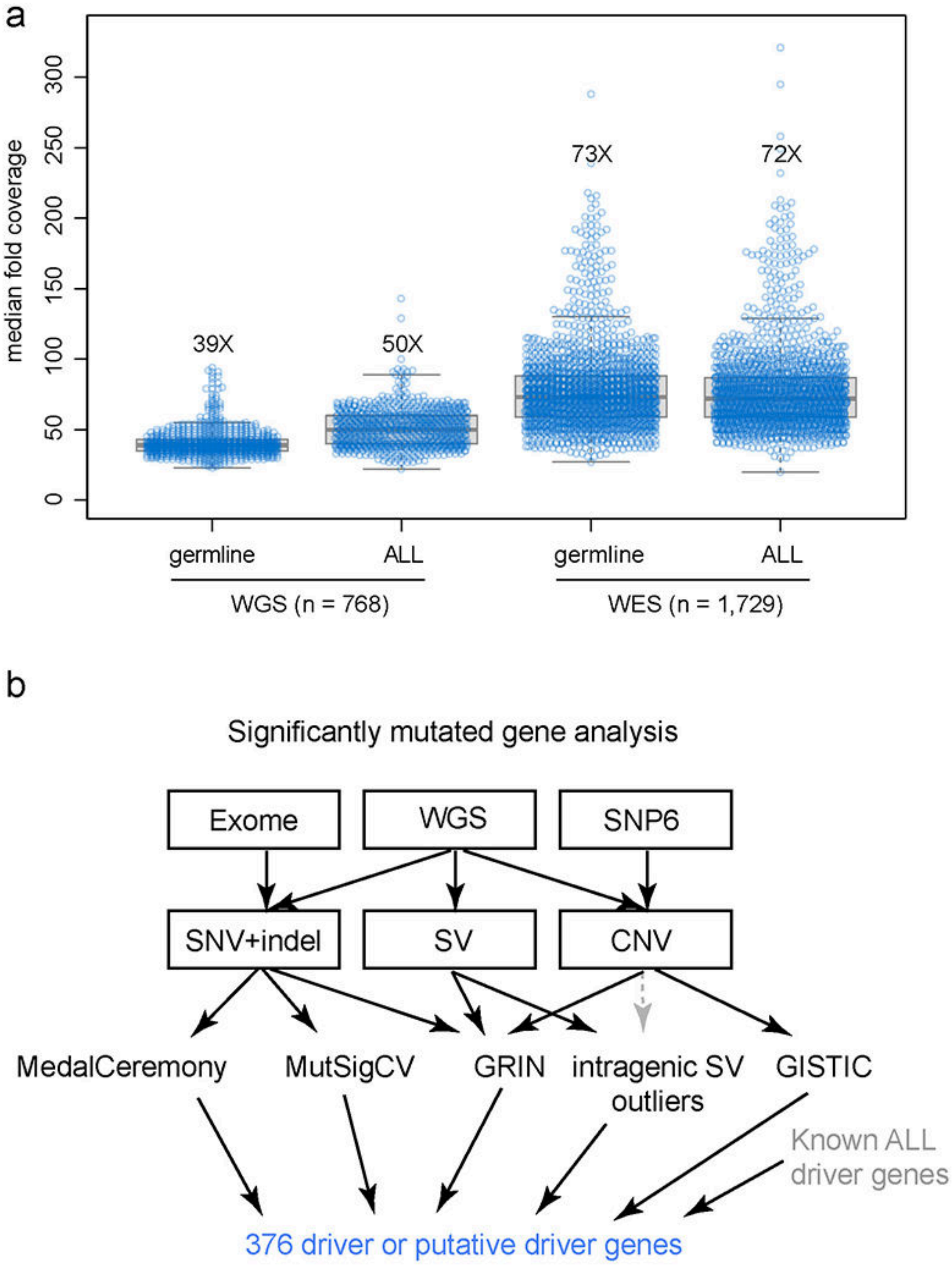

Extended Data Fig. 4. Sequencing coverage and identification of significantly mutated genes

(**a**) Each sample's median sequencing coverage based on WGS (n=768) or WES (n=1,729) is shown, including both germline and cancer (ALL) samples for each patient. Boxplot shows median (thick center line) and interquartile range (box). Whiskers are described in R boxplot documentation (a 1.5*interquartile range rule is used). The median coverage across all samples is indicated by text (e.g. "39X"). For WGS, the genome-wide coverage for each sample is indicated by each point. For WES, the median coverage in all protein-coding regions of exons (excluding 5' and 3' untranslated regions), as defined by the UCSC refGene.txt file, is shown. (**b**) Approach for identification of significantly mutated genes. The sequencing platform is shown on top, followed by the variant types detected by each platform below, and the third layer shows the tools used to identify significantly altered genes, with arrows indicating the variant types used as input to these tools. Intragenic SV outliers were identified initially by frequent SVs within the gene, and were corroborated manually with copy number analysis (dotted gray line) as the SVs were usually at the boundaries of focal deletions. All significantly mutated genes' focal deletion and SNV/indel mutation site localization were manually inspected and those considered unlikely drivers were excluded. When combining the significantly mutated genes thus identified with the list of known drivers in ALL, a list of 376 driver or putative driver genes was identified.

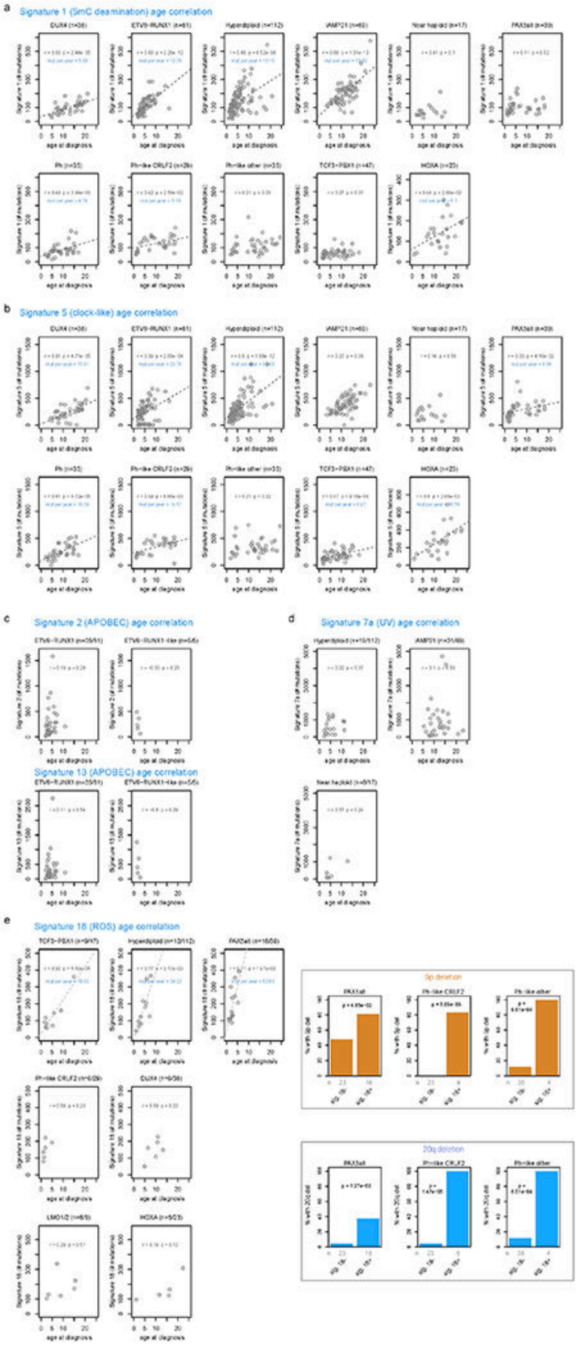

Extended Data Fig. 5. Correlation of COSMIC signatures with age and genetic alterations

For each B-ALL and T-ALL subtype, the correlation between signature abundance (in number of SNVs, y-axis) and the age at diagnosis (x-axis) is shown. This includes samples sequenced by WGS which had mutational signature cosine similarities (comparing the sample profile vs. the profile as reconstructed by signatures) of 0.85 or above, and which also had available age information. Only subtypes with at least 5 samples meeting these criteria are shown, and the number of samples in each subtype are shown above each plot. Two-sided Pearson r correlation was performed to obtain the *P* and r values shown for each subtype. For subtypes with $P < 0.05$, linear regression was performed resulting in the linear fits shown, along with text indicating the slope of the line in mutations per year. **(a)** Signature 1 (5mC deamination). **(b)** Signature 5 (clock-like). **(c)** Signatures 2 and 13 (APOBEC). **(d)** Signature 7 (UV). **(e)** Signature 18 (ROS; left). Somatic alterations significantly correlating with signature 18 (right). Each somatic alteration (chromosome-level copy alterations and driver/putative driver genes) was tested for correlation with the presence vs. absence of signature 18, and 20q deletion and 9p deletion were significantly associated with signature 18 in the subtypes shown. P values are by two-sided Fisher's exact test, and the number of samples in each group are shown below (n). Only WGS samples were analyzed.

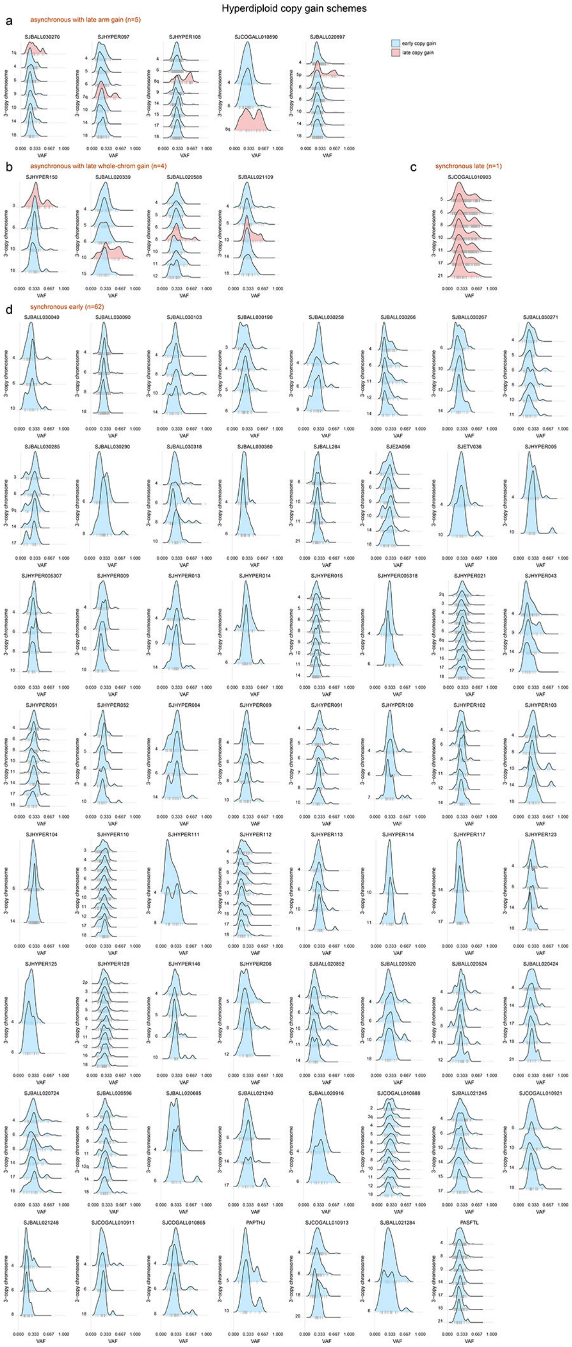

Extended Data Fig. 6. Copy gain schemes in each hyperdiploid sample.

Each hyperdiploid sample sequenced by WGS is shown. This analysis tests whether copy gains likely occurred simultaneously or sequentially and is an expanded version of the examples shown in Fig. 2d, showing all 72 samples. Only 3-copy chromosomes with at least 20 somatic SNVs in the sample were analyzed, and only samples with two or chromosomes meeting this criterion were analyzed. On density plots, x-axes show VAF adjusted for tumor purity, and y-axes show each 3-copy whole-chromosome or arm gain in the sample. Vertical ticks on x-axis show individual SNV VAFs; an abundance of VAFs around 0.67 indicates late copy gains since the SNVs occurred prior to the copy gains (2 of 3 copies), while a preponderance of VAFs around 0.33 indicates early copy gains since most SNVs occurred after the copy gains (1 of 3 copies). Blue indicates an inferred early copy gain and red a late copy gain. (**a**) Samples falling into the asynchronous with late arm gain scheme, where most copy gains occur early with one chromosome arm gain occurring later. (**b**) Samples falling into the asynchronous with whole-chromosome gain scheme, where most copy gains occur early with one whole-chromosome gain occurring later. (**c**) Lone sample belonging to the synchronous late gain scheme, where all copy gains appear to occur simultaneously and occur late, after substantial point mutations have had time to accumulate (thus present on 2 of 3 copies). (**d**) Samples belonging to the synchronous early gain scheme, where all copy gains appear to occur simultaneously and occur early, before substantial point mutations have had time to accumulate (SNVs are present on 1 of 3 copies).

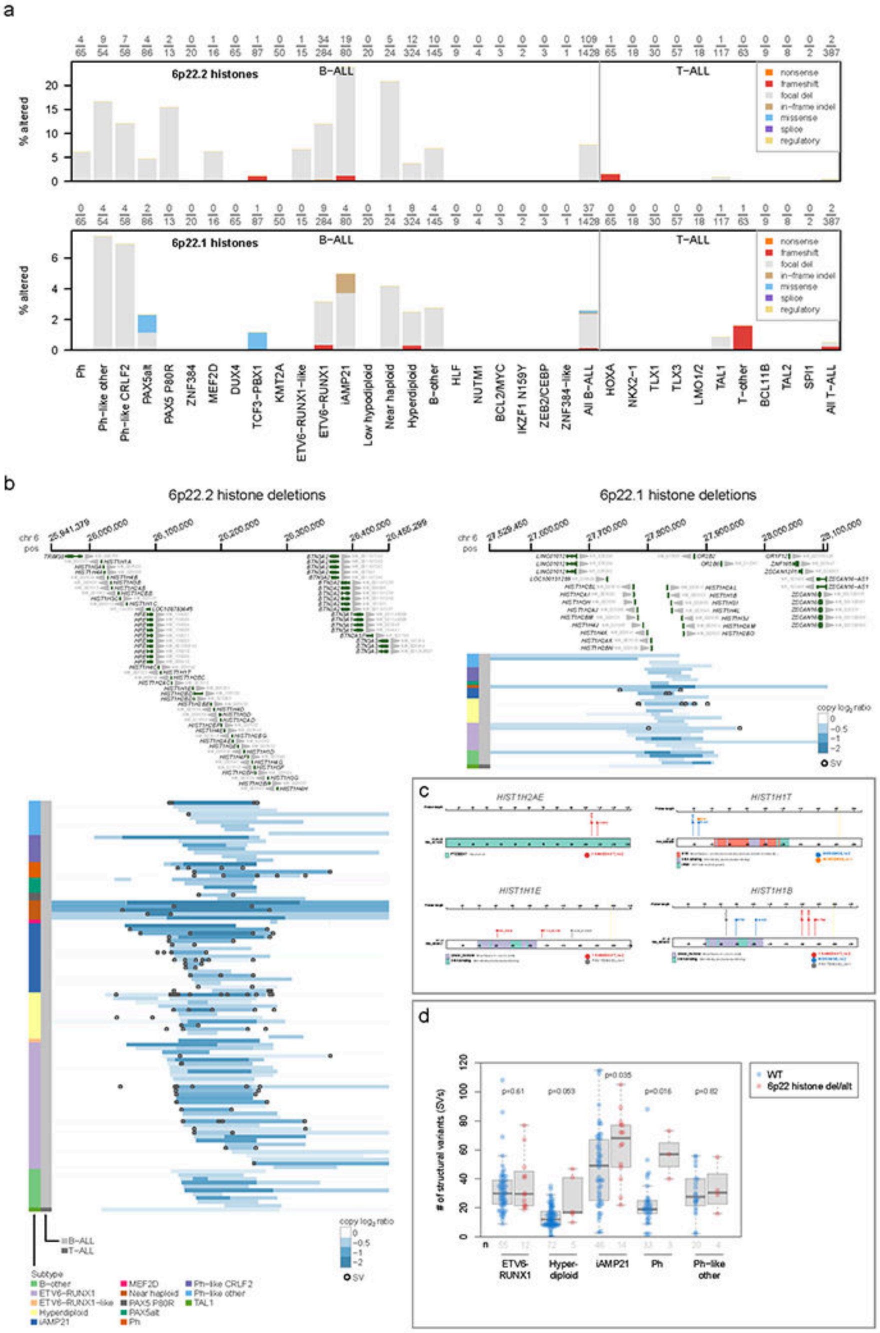

Extended Data Fig. 7. Genetic alterations affecting histone genes on chromosome 6p22.2 and 6p22.1

(**a**) Prevalence of genetic alterations affecting any of the histones on 6p22.2 (top) or 6p22.1 (bottom) in each ALL subtype. Y-axis indicates the percentage of samples affected in each subtype, and the exact number of samples altered along with the number of samples analyzed in each subtype is shown above each plot. Samples with characterisation of both SNVs/indels and copy number alterations (through WGS or WES combined with SNP array) were analyzed. Alteration types are indicated by color (see legend at top right) and exclude fusions. If a sample had an alteration in more than one histone or more than one alteration type, only one alteration at the highest rank in the legend of alterations (e.g. “nonsense” has top priority) was shown. (**b**) Focal deletions (5 Mb or less; blue indicates degree of copy loss in each sample (row) and circles indicate SVs which were available for WGS samples only) at 6p22.2 (left) or 6p22.1 (right) affecting at least one histone in either region. Color at left indicates the subtype and lineage (B-ALL or T-ALL) as indicated by legend at bottom. (**c**) Sites of non-silent SNVs and indels in histones on 6p22 which were recurrently altered. Protein domains are indicated in color. (**d**) Somatic structural variant (SV) burden in patients with or without (WT) deletion of one or more histones on 6p22.2 or 6p22.1 or other SNV/indel alterations in histone genes such as those in (**c**). Only patients with Illumina WGS data were analyzed, and only ALL subtypes with at least 3 histone-altered samples are shown. *P* values are by two-sided Wilcoxon rank-sum test. Boxplots show median (thick center line) and interquartile range (box). Whiskers are described in R boxplot documentation (a 1.5*interquartile range rule is used).

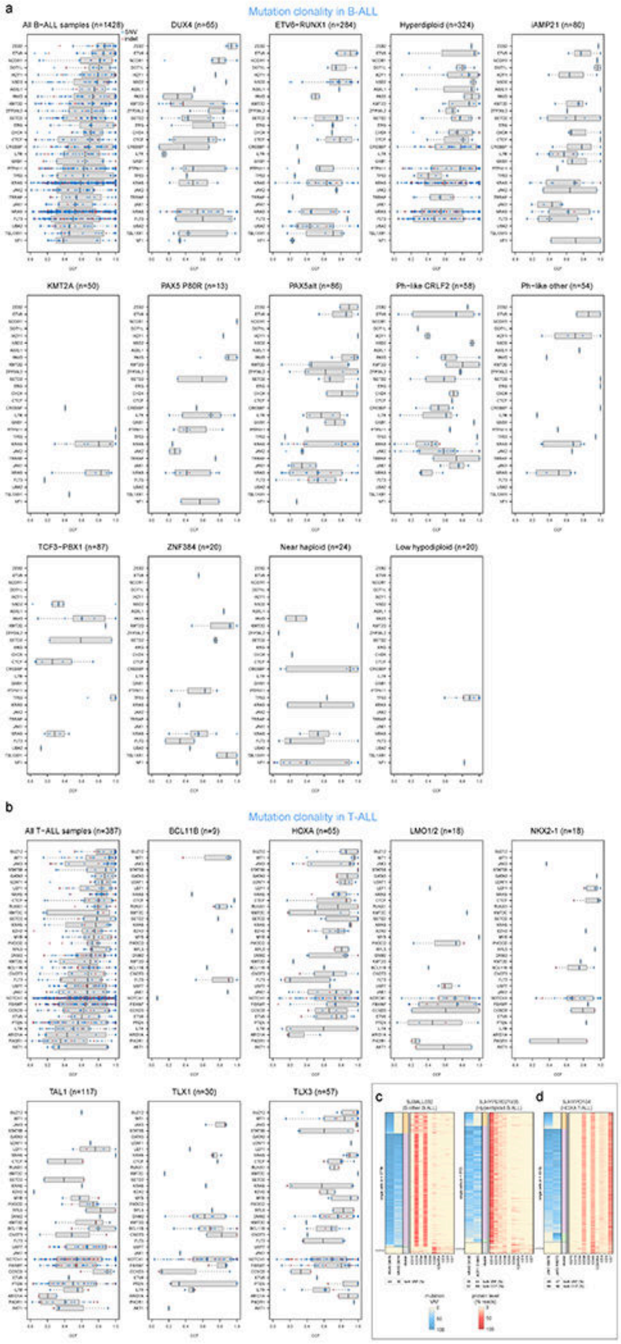

Extended Data Fig. 8. Clonality of driver SNVs and indels in B-ALL and T-ALL.

(**a**-**b**) The cancer cell fraction (CCF, x-axis), i.e. the percentage of cancer cells harboring each mutation, of alterations in each driver or putative driver gene is shown in (a) all B-ALL samples or the indicated B-ALL subtype, or (b) all T-ALL samples or the indicated T-ALL subtype. The CCF was calculated based on the VAF, copy number, and tumor purity of each sample; calculated CCFs above 1.0 were considered 1.0. Samples with both SNV/indel and copy number characterisation are shown. For subtype-specific plots, only subtypes with at least 20 samples meeting this criterion are shown. Each plot shows the number of samples analyzed (n) at top. For most samples, only SNVs/indels in 2-copy regions were analyzed, except for near haploid and low hypodiploid where only SNVs/indels in 1-copy regions were analyzed. SNVs are shown in blue and indels in red; each point represents one somatic mutation. Boxplots show median (thick center line) and interquartile range (box). Whiskers are described in R boxplot documentation (a 1.5*interquartile range rule is used). Known or putative driver genes with at least 10 SNVs/indels in 2-copy regions across all B-ALL samples, or 8 SNVs/indels in 2-copy regions across all T-ALL samples, are shown. (**c-d**) Targeted single-cell DNA sequencing plus protein analysis of two B-ALL samples (c) and one T-ALL sample (d). For each patient, a heatmap is shown with each row representing one cell, and each column representing either one mutation (left side) or one protein (right side). Mutation VAF is indicated by blue color, while protein level (as a percent of all protein-associated reads detected in the cell) is indicated by red color. At bottom of heatmap likely normal cells are indicated. The bulk VAF of each mutation is indicated below, along with bulk CCF (if copy number was available).

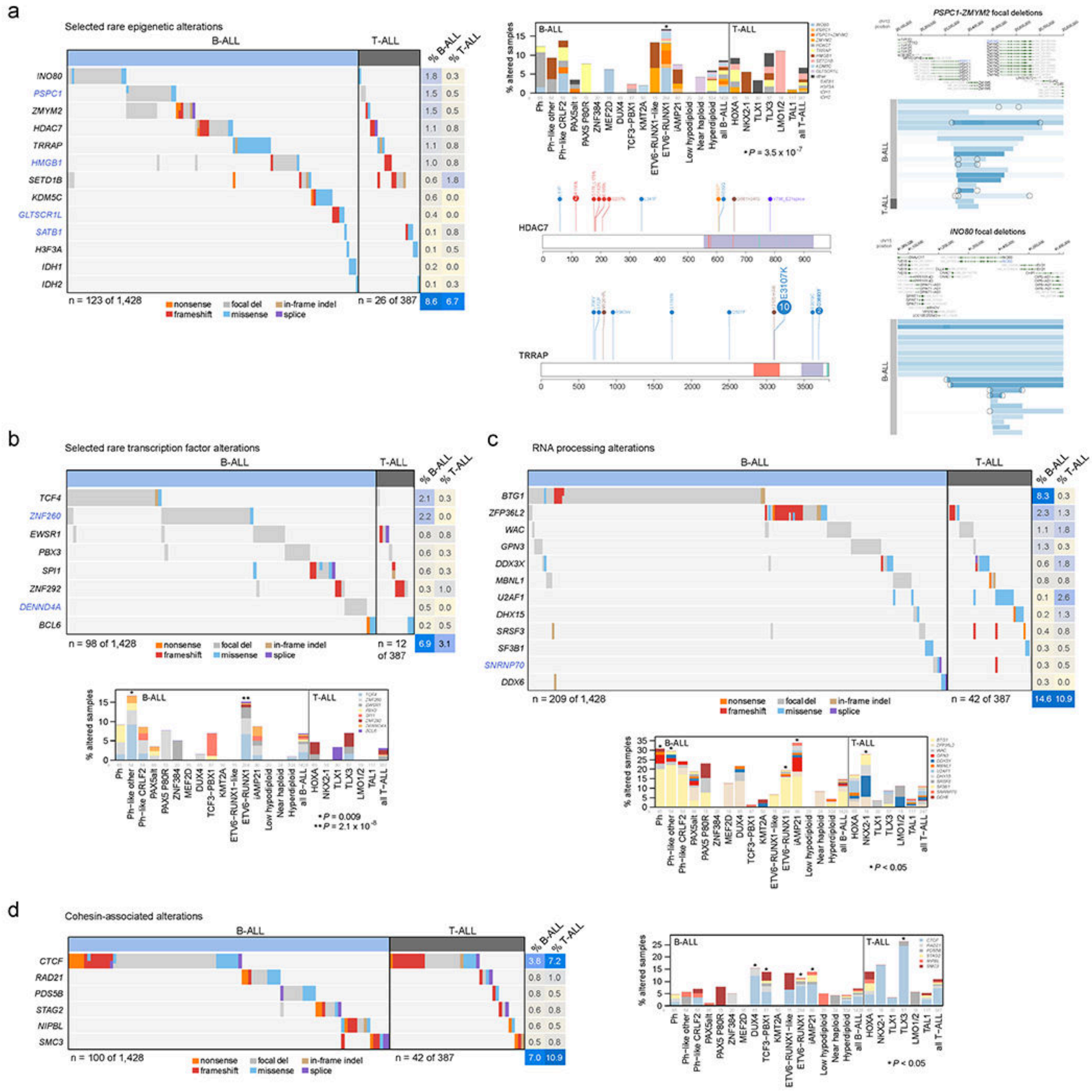

Extended Data Fig. 9. Alterations in rarely mutated genes affecting gene expression.

(**a**) Selected alterations in rare epigenetic modulators. Putative cancer driver genes are shown in blue text. Left shows an oncoprint showing only samples with alterations in at least one of these genes, with alteration type indicated by color and the percentage of samples in B-ALL or T-ALL altered at right. Top-middle shows the percentage of each subtype with alterations in these genes, color-coded by the specific gene altered. In samples with alterations with more than one gene, only the top-most gene in the legend is shown. Number of samples in each subtype is as in Fig. 5b. Right shows example gene alterations, including focal deletions (5 Mb or less; blue indicates degree of copy loss in each sample (row) and circles indicate SVs which were available for WGS samples only) in *PSPC1-ZMYM2* and *INO80.* Sites of sequence alterations in *HDAC7* and *TRRAP* are shown at middle-bottom. (**b-d**) Oncoprints and subtype bar plots as in (a) except that shown are selected transcription factors (b), RNA processing factors (c), and cohesion-associated genes (d). *P* values (asterisks) are by two-sided Fisher's exact test comparing prevalence in the indicated subtype vs. all samples not belonging to that subtype (within that lineage (B-ALL or T-ALL), so that ETV6-RUNX1 subtype would be compared to B-ALL samples of other subtypes, while TLX3 subtype would be compared to T-ALL samples of other subtypes). In (c), exact *P* values are 8.6 x 10^{-4} (Ph), 0.0047 (Ph-like other), 0.015 (ETV6-RUNX1), 9.7 x 10^{-6} (iAMP21), and 0.035 (NKX2-1). In (d), exact *P* values are 0.020 (DUX4), 0.016 (TCF3-PBX1), 0.0027 (ETV6-RUNX1), 0.023 (iAMP21), and 2.6 x 10^{-4} (TLX3).

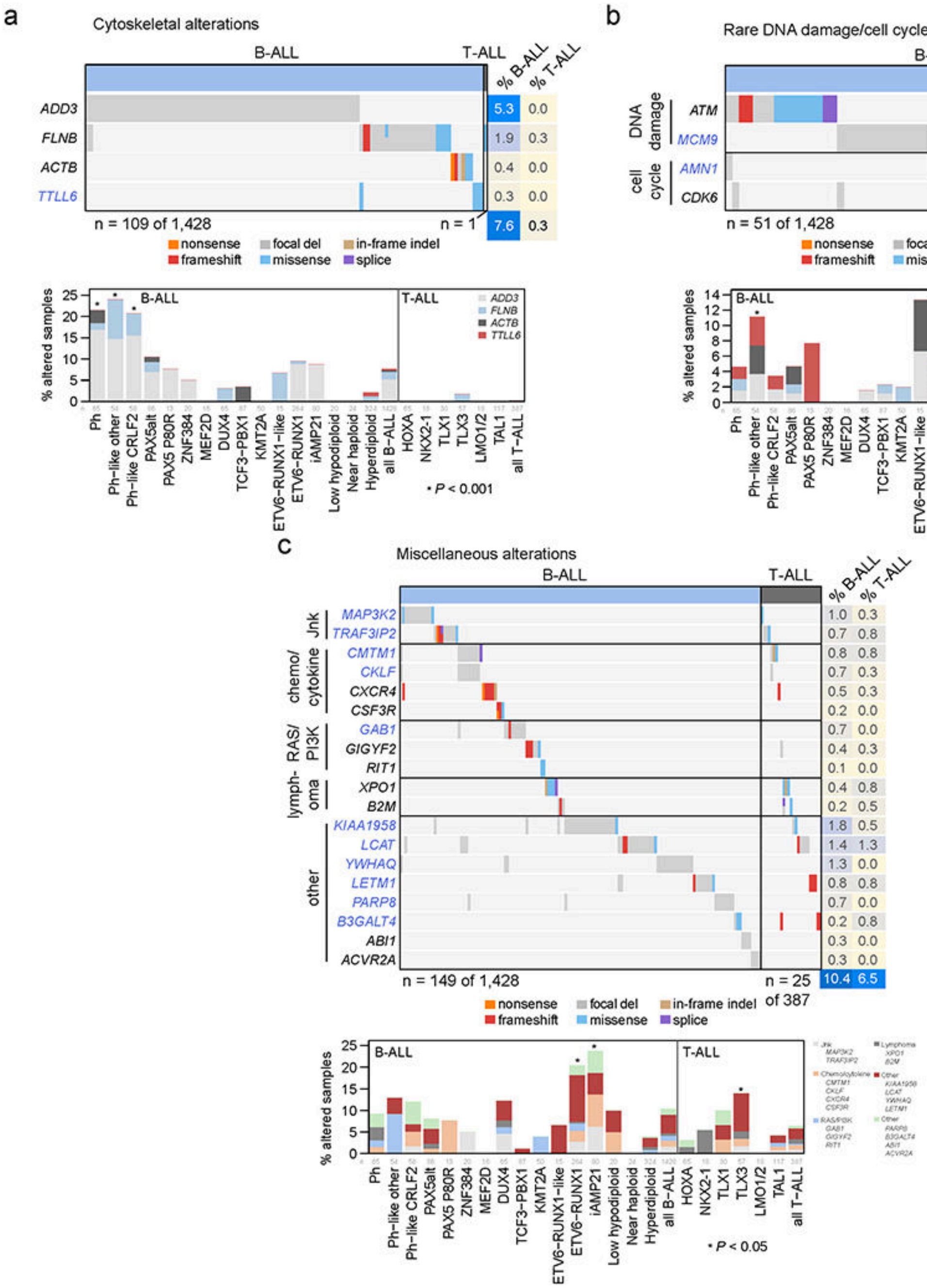

Extended Data Fig. 10. Alterations in rarely mutated genes affecting the cytoskeleton and other miscellaneous alterations

(**a**) Selected alterations in cytoskeleton-related genes. Putative cancer driver genes are shown in blue text. Top shows an oncoprint showing only samples with alterations in at least one of these genes, with alteration type indicated by color and the percentage of samples in B-ALL or T-ALL altered at right. Bottom shows the percentage of each subtype with alterations in these genes, color-coded by the specific gene altered. In samples with alterations with more than one gene, only the top-most gene in the legend is shown. Number of samples in each subtype is as in Fig. 5b. (**b**-**c**) Oncoprints and subtype bar plots as in (a) except that shown are selected rare alterations affecting DNA damage or the cell cycle (b), and miscellaneous alterations affecting various pathways as indicated by text to the left (c). *P* values (asterisks) are by two-sided Fisher's exact test comparing prevalence in the indicated subtype vs. all samples not belonging to that subtype (within that lineage (B-ALL or T-ALL), so that ETV6-RUNX1 subtype would be compared to B-ALL samples of other subtypes, while TLX3 subtype would be compared to T-ALL samples of other subtypes). In (a), exact *P* values are 2.2 x 10^{-4} (Ph), 1.1 x 10^{-4} (Ph-like other), and 9.5 x 10^{-4} (Ph-like CRLF2). In (b), exact *P* values are 0.011 (Ph-like other), and 0.048 (ETV6-RUNX1). In (c), exact *P* values are 1.4 x 10^{-8} (ETV6-RUNX1), 4.2 x 10^{-4} (iAMP21), and 0.019 (TLX3).

Supplementary Material

Refer to Web version on PubMed Central for supplementary material.

Authors

Samuel W. Brady[1,*], Kathryn G. Roberts[2,*], Zhaohui Gu[3], Lei Shi[4], Stanley Pounds[4], Deqing Pei[4], Cheng Cheng[4], Yunfeng Dai[5], Meenakshi Devidas[6], Chunxu Qu[2], Ashley N. Hill[2], Debbie Payne-Turner[2], Xiaotu Ma[1], Ilaria Iacobucci[2], Pradyuamna Baviskar[2], Lei Wei[1], Sasi Arunachalam[1], Kohei Hagiwara[1], Yanling Liu[1], Diane A. Flasch[1], Yu Liu[1], Matthew Parker[1], Xiaolong Chen[1], Abdelrahman H. Elsayed[2,4], Omkar Pathak[1], Yongjin Li[1], Yiping Fan[1], J. Robert Michael[1], Michael Rusch[1], Mark R. Wilkinson[1], Scott Foy[1], Dale Hedges[1], Scott Newman[1], Xin Zhou[1], Jian Wang[1], Colleen Reilly[1], Edgar Sioson[1], Stephen V. Rice[1], Victor Pastor Loyola[1], Gang Wu[7], Evadnie Rampersaud[7], Shalini C. Reshmi[8], Julie Gastier-Foster[9], Jaime M. Guidry-Auvil[10], Patee Gesuwan[10], Malcolm A. Smith[11], Naomi Winick[12], Andrew J. Carroll[13], Nyla A. Heerema[14], Richard C. Harvey[15], Cheryl L. Willman[16], Eric Larsen[17], Elizabeth A. Raetz[18], Michael J. Borowitz[19], Brent L. Wood[20], William L. Carroll[18], Patrick A. Zweidler-McKay[21], Karen R. Rabin[9], Leonard A. Mattano[22], Kelly W. Maloney[23], Stuart S. Winter[24], Michael J. Burke[25], Wanda Salzer[26], Kimberley P. Dunsmore[27], Anne L. Angiolillo[28], Kristine R. Crews[29], James R. Downing[2], Sima Jeha[30], Ching-Hon Pui[30], William E. Evans[29], Jun J. Yang[29], Mary V. Relling[29], Daniela S. Gerhard[10,¶], Mignon L. Loh[31], Stephen P. Hunger[32,**], Jinghui Zhang[1,**], Charles Mullighan[2,**]

Affiliations

[1]Department of Computational Biology, St. Jude Children's Research Hospital, Memphis TN, USA

[2]Department of Pathology, St. Jude Children's Research Hospital, Memphis TN, USA

[3]Department of Computational and Quantitative Medicine & Systems Biology, Beckman Research Institute of City of Hope, Duarte CA, USA

[4]Department of Biostatistics, St. Jude Children's Research Hospital, Memphis TN, USA

[5]Department of Biostatistics, University of Florida, Gainesville FL, USA

[6]Department of Global Pediatric Medicine, St. Jude Children's Research Hospital, Memphis TN, USA

[7]Center for Applied Bioinformatics, St. Jude Children's Research Hospital, Memphis TN, USA

[8]Institute for Genomic Medicine, Nationwide Children's Hospital, Columbus OH, USA

[9]Department of Pediatrics, Baylor College of Medicine, Houston TX, USA

[10]Office of Cancer Genomics, National Cancer Institute, National Institutes of Health, Bethesda MD, USA

[11]Cancer Therapeutics Evaluation Program, National Cancer Institute, National Institutes of Health, Bethesda MD, USA

[12]Department of Pediatric Hematology Oncology and Simmons Cancer Center, University of Texas Southwestern Medical Center, Dallas TX, USA

[13]Department of Genetics, University of Alabama at Birmingham, Birmingham AL, USA

[14]The Ohio State University, Columbus OH, USA

[15]Department of Pathology, University of New Mexico Cancer Center, Albuquerque NM, USA

[16]Mayo Clinical Comprehensive Cancer Center, Rochester, MN

[17]Department of Pediatrics, Maine Children's Cancer Program, Scarborough ME, USA

[18]Department of Pediatrics and Perlmutter Cancer Center, New York University Langone Medical Center, New York NY, USA

[19]Department of Pathology, Johns Hopkins Medical Institutions, Baltimore MD, USA

[20]Department of Pathology and Laboratory Medicine, Children's Hospital Los Angeles, University of Southern California, CA, USA

[21]ImmunoGen, Inc., Waltham MA, USA

[22]HARP Pharma Consulting, Mystic CT, USA

[23]Department of Pediatrics and Children's Hospital Colorado, University of Colorado, Aurora CO, USA

[24]Children's Minnesota Research Institute and Cancer and Blood Disorders Program, Minneapolis MN, USA

[25]Division of Pediatric Hematology-Oncology, Medical College of Wisconsin, Milwaukee WI, USA

[26]Uniformed Services University, School of Medicine, Bethesda, MD, USA

[27]Department of Pediatrics, University of Virginia, Charlottesville, VA, USA

[28]Children's National Medical Center, Washington DC, USA

[29]Department of Pharmacy and Pharmaceutical Sciences, St. Jude Children's Research Hospital, Memphis TN, USA

[30]Department of Oncology, St. Jude Children's Research Hospital, Memphis TN, USA

[31]Department of Pediatrics, Benioff Children's Hospital and Helen Diller Family Comprehensive Cancer Center, University of California, San Francisco CA, USA

[32]Department of Pediatrics and the Center for Childhood Cancer Research, Children's Hospital of Philadelphia, and the Perelman School of Medicine at the University of Pennsylvania, Philadelphia PA, USA

Acknowledgements

We thank the Biorepository, the Genome Sequencing Facility of the Hartwell Center for Bioinformatics and Biotechnology, the Flow Cytometry and Cell Sorting Shared Resource and Cytogenetics core facility of St. Jude Children's Research Hospital (SJCRH). We thank L Hermida and T Davidsen for assistance with genomic data management. This work was supported by the American Lebanese Syrian Associated Charities of SJCRH, St. Baldricks Foundation Robert J. Arceci Innovation Award (to C.G.M.), Alex's Lemonade Stand Foundation Innovation Award (to C.G.M.), American Society of Hematology Scholar Award (to Z.G.), The Leukemia & Lymphoma Society's Career Development Program Special Fellow (to Z.G.), National Cancer Institute grants P30 CA021765 (SJCRH Cancer Center Support Grant), Outstanding Investigator Award R35 CA197695 (to C.G.M.), R01 CA216391 (to J.Z.) and Pathway to Independence Award R00 CA241297 (to Z.G.), National Institute of General Medical Sciences P50 GM115279 (to M.V.R., C.G.M., J.Y., M.L.L., W.E.E., J.Z. and C.C.) and St. Baldricks Foundation Award (to M.L.L and S.P.H). C.G.M. is the William E. Evans Endowed Chair at SJCRH. This study is dedicated to the memory of Daniela S. Gerhard.

Competing interests statement

C.G.M. has received consulting and speaking fees from Illumina and Amgen, and research support from Loxo Oncology, Pfizer and Abbvie. M.J.B. is on the advisory board for Amgen and Blueprint Medicines. I.I. has received honoraria from Amgen and Mission Bio. M.P. is an employee of Oxford Nanopore Technologies P.L.C.. J.J.Y. has received research funding from Takeda Pharmaceuticals. The remaining authors declare no competing interests.

Main References

1. Iacobucci I, Kimura S & Mullighan CG Biologic and Therapeutic Implications of Genomic Alterations in Acute Lymphoblastic Leukemia. J Clin Med 10, 3792 (2021). [PubMed: 34501239]
2. Roberts KG & Mullighan CG The Biology of B-Progenitor Acute Lymphoblastic Leukemia. Cold Spring Harb Perspect Med 10(2020).
3. Den Boer ML et al. A subtype of childhood acute lymphoblastic leukaemia with poor treatment outcome: a genome-wide classification study. Lancet Oncol 10, 125–34 (2009). [PubMed: 19138562]
4. Mullighan CG et al. Deletion of IKZF1 and prognosis in acute lymphoblastic leukemia. N Engl J Med 360, 470–80 (2009). [PubMed: 19129520]
5. Roberts KG Why and how to treat Ph-like ALL? Best Pract Res Clin Haematol 31, 351–356 (2018). [PubMed: 30466746]
6. Tasian SK, Loh ML & Hunger SP Philadelphia chromosome-like acute lymphoblastic leukemia. Blood 130, 2064–2072 (2017). [PubMed: 28972016]
7. Lilljebjorn H et al. Identification of ETV6-RUNX1-like and DUX4-rearranged subtypes in paediatric B-cell precursor acute lymphoblastic leukaemia. Nat Commun 7, 11790 (2016). [PubMed: 27265895]

8. Zhang J et al. Deregulation of DUX4 and ERG in acute lymphoblastic leukemia. Nat Genet 48, 1481–1489 (2016). [PubMed: 27776115]

9. Gu Z et al. Genomic analyses identify recurrent MEF2D fusions in acute lymphoblastic leukaemia. Nat Commun 7, 13331 (2016). [PubMed: 27824051]

10. Gocho Y et al. A novel recurrent EP300-ZNF384 gene fusion in B-cell precursor acute lymphoblastic leukemia. Leukemia 29, 2445–8 (2015). [PubMed: 25943178]

11. Lilljebjorn H & Fioretos T New oncogenic subtypes in pediatric B-cell precursor acute lymphoblastic leukemia. Blood 130, 1395–1401 (2017). [PubMed: 28778863]

12. Bastian L et al. PAX5 biallelic genomic alterations define a novel subgroup of B-cell precursor acute lymphoblastic leukemia. Leukemia 33, 1895–1909 (2019). [PubMed: 30842609]

13. Passet M et al. PAX5 P80R mutation identifies a novel subtype of B-cell precursor acute lymphoblastic leukemia with favorable outcome. Blood 133, 280–284 (2019). [PubMed: 30510083]

14. Gu Z et al. PAX5-driven subtypes of B-progenitor acute lymphoblastic leukemia. Nat Genet 51, 296–307 (2019). [PubMed: 30643249]

15. Li JF et al. Transcriptional landscape of B cell precursor acute lymphoblastic leukemia based on an international study of 1,223 cases. Proc Natl Acad Sci U S A 115, E11711–e11720 (2018). [PubMed: 30487223]

16. Ueno H et al. Landscape of driver mutations and their clinical impacts in pediatric B-cell precursor acute lymphoblastic leukemia. Blood Adv 4, 5165–5173 (2020). [PubMed: 33095873]

17. Liu Y et al. The genomic landscape of pediatric and young adult T-lineage acute lymphoblastic leukemia. Nat Genet 49, 1211–1218 (2017). [PubMed: 28671688]

18. Jeha S et al. Clinical significance of novel subtypes of acute lymphoblastic leukemia in the context of minimal residual disease-directed therapy. Blood Cancer Discov 2, 326–337 (2021).

19. Montefiori LE et al. Enhancer Hijacking Drives Oncogenic BCL11B Expression in Lineage-Ambiguous Stem Cell Leukemia. Cancer Discov 11, 2846–2867 (2021). [PubMed: 34103329]

20. Lawrence MS et al. Mutational heterogeneity in cancer and the search for new cancer-associated genes. Nature 499, 214–218 (2013). [PubMed: 23770567]

21. Pounds S et al. A genomic random interval model for statistical analysis of genomic lesion data. Bioinformatics 29, 2088–95 (2013). [PubMed: 23842812]

22. Mermel CH et al. GISTIC2.0 facilitates sensitive and confident localization of the targets of focal somatic copy-number alteration in human cancers. Genome Biol 12, R41 (2011). [PubMed: 21527027]

23. Edmonson MN et al. Pediatric Cancer Variant Pathogenicity Information Exchange (PeCanPIE): a cloud-based platform for curating and classifying germline variants. Genome Res 29, 1555–1565 (2019). [PubMed: 31439692]

24. Ma X et al. Pan-cancer genome and transcriptome analyses of 1,699 paediatric leukaemias and solid tumours. Nature 555, 371–376 (2018). [PubMed: 29489755]

25. Sondka Z et al. The COSMIC Cancer Gene Census: describing genetic dysfunction across all human cancers. Nat Rev Cancer 18, 696–705 (2018). [PubMed: 30293088]

26. ICGC/TCGA Pan-Cancer Analysis of Whole Genomes Consortium. Pan-cancer analysis of whole genomes. Nature 578, 82–93 (2020). [PubMed: 32025007]

27. Alexandrov LB et al. The repertoire of mutational signatures in human cancer. Nature 578, 94–101 (2020). [PubMed: 32025018]

28. Alexandrov LB et al. Clock-like mutational processes in human somatic cells. Nat Genet 47, 1402–7 (2015). [PubMed: 26551669]

29. Petljak M et al. Characterizing Mutational Signatures in Human Cancer Cell Lines Reveals Episodic APOBEC Mutagenesis. Cell 176, 1282–1294 e20 (2019). [PubMed: 30849372]

30. Maia AT et al. Prenatal origin of hyperdiploid acute lymphoblastic leukemia in identical twins. Leukemia 17, 2202–6 (2003). [PubMed: 12931229]

31. Li Y et al. Constitutional and somatic rearrangement of chromosome 21 in acute lymphoblastic leukaemia. European Journal of Cancer 50, S97–S97 (2014).

32. Albig W et al. All known human H1 histone genes except the H1(0) gene are clustered on chromosome 6. Genomics 16, 649–54 (1993). [PubMed: 8325638]

33. Albig W, Trappe R, Kardalinou E, Eick S & Doenecke D The human H2A and H2B histone gene complement. Biol Chem 380, 7–18 (1999). [PubMed: 10064132]

34. Ederveen TH, Mandemaker IK & Logie C The human histone H3 complement anno 2011. Biochim Biophys Acta 1809, 577–86 (2011). [PubMed: 21782046]

35. Miles DM, Desdouets C & Geli V Histone stress: an unexplored source of chromosomal instability in cancer? Curr Genet 65, 1081–1088 (2019). [PubMed: 30976832]

36. Elia MC & Bradley MO Influence of chromatin structure on the induction of DNA double strand breaks by ionizing radiation. Cancer Res 52, 1580–6 (1992). [PubMed: 1540967]

37. Rosidi B et al. Histone H1 functions as a stimulatory factor in backup pathways of NHEJ. Nucleic Acids Res 36, 1610–23 (2008). [PubMed: 18250087]

38. Li Y et al. Constitutional and somatic rearrangement of chromosome 21 in acute lymphoblastic leukaemia. Nature 508, 98–102 (2014). [PubMed: 24670643]

39. Jerchel IS et al. RAS pathway mutations as a predictive biomarker for treatment adaptation in pediatric B-cell precursor acute lymphoblastic leukemia. Leukemia 32, 931–940 (2018). [PubMed: 28972594]

40. Mullighan CG et al. Genome-wide analysis of genetic alterations in acute lymphoblastic leukaemia. Nature 446, 758–64 (2007). [PubMed: 17344859]

41. Weng AP et al. Activating mutations of NOTCH1 in human T cell acute lymphoblastic leukemia. Science 306, 269–71 (2004). [PubMed: 15472075]

42. Sulong S et al. A comprehensive analysis of the CDKN2A gene in childhood acute lymphoblastic leukemia reveals genomic deletion, copy number neutral loss of heterozygosity, and association with specific cytogenetic subgroups. Blood 113, 100–7 (2009). [PubMed: 18838613]

43. Gutierrez A et al. High frequency of PTEN, PI3K, and AKT abnormalities in T-cell acute lymphoblastic leukemia. Blood 114, 647–50 (2009). [PubMed: 19458356]

44. Holmfeldt L et al. The genomic landscape of hypodiploid acute lymphoblastic leukemia. Nat Genet 45, 242–52 (2013). [PubMed: 23334668]

45. Tarabichi M et al. A practical guide to cancer subclonal reconstruction from DNA sequencing. Nat Methods 18, 144–155 (2021). [PubMed: 33398189]

46. Okuma T, Honda R, Ichikawa G, Tsumagari N & Yasuda H In vitro SUMO-1 modification requires two enzymatic steps, E1 and E2. Biochem Biophys Res Commun 254, 693–8 (1999). [PubMed: 9920803]

47. Lammer F, Klaumuenzer M, Mossner M & Jann JC Next Generation RNA Sequencing of Acute Promyelocytic Leukemia (APL) Identifies Novel Long Non Coding RNAs Including New Variants of MIR181A1HG That Are Differentially Expressed during Myeloid Differentiation. Blood (ASH abstract) 124, 1031 (2014).

48. Armenia J et al. The long tail of oncogenic drivers in prostate cancer. Nat Genet 50, 645–651 (2018). [PubMed: 29610475]

49. Stanulla M et al. IKZF1(plus) Defines a New Minimal Residual Disease-Dependent Very-Poor Prognostic Profile in Pediatric B-Cell Precursor Acute Lymphoblastic Leukemia. J Clin Oncol 36, 1240–1249 (2018). [PubMed: 29498923]

50. Hystad ME et al. Characterization of early stages of human B cell development by gene expression profiling. J Immunol 179, 3662–71 (2007). [PubMed: 17785802]

51. Guo H, Barberi T, Suresh R & Friedman AD Progression from the Common Lymphoid Progenitor to B/Myeloid PreproB and ProB Precursors during B Lymphopoiesis Requires C/EBPalpha. J Immunol 201, 1692–1704 (2018). [PubMed: 30061199]

52. Consortium, I.T.P.-C.A.o.W.G. Pan-cancer analysis of whole genomes. Nature 578, 82–93 (2020). [PubMed: 32025007]

53. Mullighan CG et al. BCR-ABL1 lymphoblastic leukaemia is characterized by the deletion of Ikaros. Nature 453, 110–4 (2008). [PubMed: 18408710]

54. Papaemmanuil E et al. RAG-mediated recombination is the predominant driver of oncogenic rearrangement in ETV6-RUNX1 acute lymphoblastic leukemia. Nat Genet 46, 116–25 (2014). [PubMed: 24413735]
55. Heerema NA et al. Specific extra chromosomes occur in a modal number dependent pattern in pediatric acute lymphoblastic leukemia. Genes Chromosomes Cancer 46, 684–93 (2007). [PubMed: 17431878]
56. Paulsson K et al. The genomic landscape of high hyperdiploid childhood acute lymphoblastic leukemia. Nat Genet 47, 672–6 (2015). [PubMed: 25961940]
57. Alpar D et al. Sequential and hierarchical chromosomal changes and chromosome instability are distinct features of high hyperdiploid pediatric acute lymphoblastic leukemia. Pediatr Blood Cancer 61, 2208–14 (2014). [PubMed: 25174722]
58. Kucab JE et al. A Compendium of Mutational Signatures of Environmental Agents. Cell 177, 821–836 e16 (2019). [PubMed: 30982602]
59. Nielsen KP, Zhao L, Stamnes JJ, Stamnes K & Moan J The importance of the depth distribution of melanin in skin for DNA protection and other photobiological processes. J Photochem Photobiol B 82, 194–8 (2006). [PubMed: 16388960]
60. Maia AT et al. Identification of preleukemic precursors of hyperdiploid acute lymphoblastic leukemia in cord blood. Genes Chromosomes Cancer 40, 38–43 (2004). [PubMed: 15034866]
61. Jones CL et al. Spectrum of mutational signatures in T-cell lymphoma reveals a key role for UV radiation in cutaneous T-cell lymphoma. Scientific Reports 11(2021).
62. Ma X et al. Rise and fall of subclones from diagnosis to relapse in pediatric B-acute lymphoblastic leukaemia. Nat Commun 6, 6604 (2015). [PubMed: 25790293]
63. Brown PA et al. FLT3 inhibitor lestaurtinib plus chemotherapy for newly diagnosed KMT2A-rearranged infant acute lymphoblastic leukemia: Children's Oncology Group trial AALL0631. Leukemia 35, 1279–1290 (2021). [PubMed: 33623141]
64. Petit A et al. Oncogenetic mutations combined with MRD improve outcome prediction in pediatric T-cell acute lymphoblastic leukemia. Blood 131, 289–300 (2018). [PubMed: 29051182]

Methods References

65. Pui CH et al. Treating childhood acute lymphoblastic leukemia without cranial irradiation. N Engl J Med 360, 2730–41 (2009). [PubMed: 19553647]
66. Jeha S et al. Improved CNS Control of Childhood Acute Lymphoblastic Leukemia Without Cranial Irradiation: St Jude Total Therapy Study 16. J Clin Oncol 37, 3377–3391 (2019). [PubMed: 31657981]
67. Bowman WP et al. Augmented therapy improves outcome for pediatric high risk acute lymphocytic leukemia: results of Children's Oncology Group trial P9906. Pediatr Blood Cancer 57, 569–77 (2011). [PubMed: 21360654]
68. Larsen EC et al. Dexamethasone and High-Dose Methotrexate Improve Outcome for Children and Young Adults With High-Risk B-Acute Lymphoblastic Leukemia: A Report From Children's Oncology Group Study AALL0232. J Clin Oncol 34, 2380–8 (2016). [PubMed: 27114587]
69. Salzer WL et al. Impact of Intrathecal Triple Therapy Versus Intrathecal Methotrexate on Disease-Free Survival for High-Risk B-Lymphoblastic Leukemia: Children's Oncology Group Study AALL1131. J Clin Oncol 38, 2628–2638 (2020). [PubMed: 32496902]
70. Maloney KW et al. Outcome in Children With Standard-Risk B-Cell Acute Lymphoblastic Leukemia: Results of Children's Oncology Group Trial AALL0331. J Clin Oncol 38, 602–612 (2020). [PubMed: 31825704]
71. Angiolillo AL et al. Excellent Outcomes With Reduced Frequency of Vincristine and Dexamethasone Pulses in Standard-Risk B-Lymphoblastic Leukemia: Results From Children's Oncology Group AALL0932. J Clin Oncol 39, 1437–1447 (2021). [PubMed: 33411585]
72. Winter SS et al. Improved Survival for Children and Young Adults With T-Lineage Acute Lymphoblastic Leukemia: Results From the Children's Oncology Group AALL0434 Methotrexate Randomization. J Clin Oncol 36, 2926–2934 (2018). [PubMed: 30138085]

73. Wang J et al. CREST maps somatic structural variation in cancer genomes with base-pair resolution. Nat Methods 8, 652–4 (2011). [PubMed: 21666668]

74. Wala JA et al. SvABA: genome-wide detection of structural variants and indels by local assembly. Genome Res 28, 581–591 (2018). [PubMed: 29535149]

75. Chen X et al. Manta: rapid detection of structural variants and indels for germline and cancer sequencing applications. Bioinformatics 32, 1220–2 (2016). [PubMed: 26647377]

76. Rausch T et al. DELLY: structural variant discovery by integrated paired-end and split-read analysis. Bioinformatics 28, i333–i339 (2012). [PubMed: 22962449]

77. Li Y et al. Patterns of somatic structural variation in human cancer genomes. Nature 578, 112–121 (2020). [PubMed: 32025012]

78. Edmonson MN et al. Bambino: a variant detector and alignment viewer for next-generation sequencing data in the SAM/BAM format. Bioinformatics 27, 865–6 (2011). [PubMed: 21278191]

79. McLaren W et al. The Ensembl Variant Effect Predictor. Genome Biol 17, 122 (2016). [PubMed: 27268795]

80. Wang K, Li M & Hakonarson H ANNOVAR: functional annotation of genetic variants from high-throughput sequencing data. Nucleic Acids Res 38, e164 (2010). [PubMed: 20601685]

81. Ioannidis NM et al. REVEL: An Ensemble Method for Predicting the Pathogenicity of Rare Missense Variants. Am J Hum Genet 99, 877–885 (2016). [PubMed: 27666373]

82. Zhou X et al. Exploring genomic alteration in pediatric cancer using ProteinPaint. Nat Genet 48, 4–6 (2016). [PubMed: 26711108]

83. Yang M et al. 13q12.2 deletions in acute lymphoblastic leukemia lead to upregulation of FLT3 through enhancer hijacking. Blood 136, 946–956 (2020). [PubMed: 32384149]

84. Alexandrov LB et al. Signatures of mutational processes in human cancer. Nature 500, 415–21 (2013). [PubMed: 23945592]

85. Li B et al. Therapy-induced mutations drive the genomic landscape of relapsed acute lymphoblastic leukemia. Blood 135, 41–55 (2020). [PubMed: 31697823]

86. Alberti-Servera L et al. Single-cell DNA amplicon sequencing reveals clonal heterogeneity and evolution in T-cell acute lymphoblastic leukemia. Blood 137, 801–811 (2021). [PubMed: 32812017]

87. Zhou X et al. Exploration of Coding and Non-coding Variants in Cancer Using GenomePaint. Cancer Cell 39, 83–95 e4 (2021). [PubMed: 33434514]

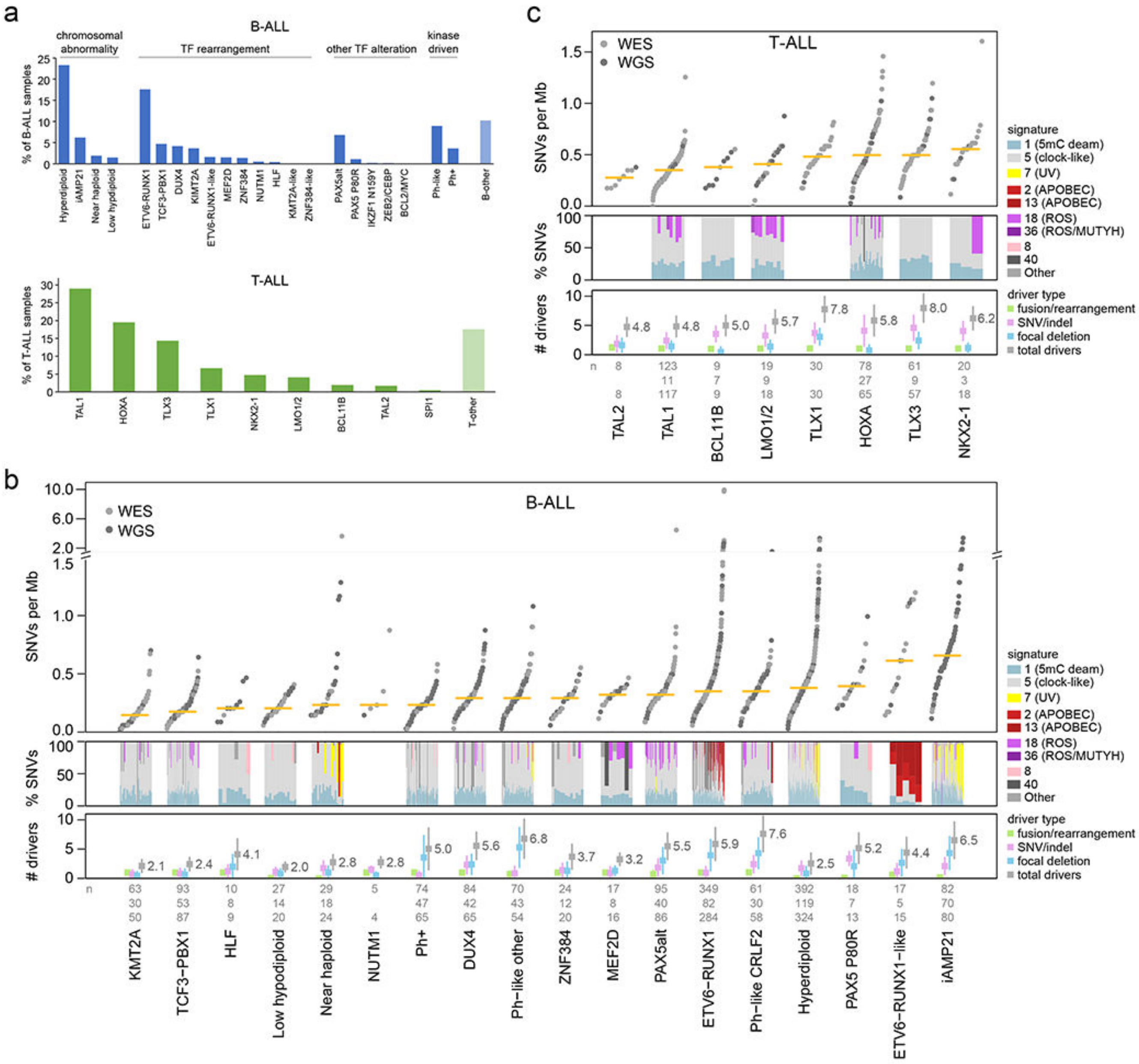

Figure 1. ALL cohort, mutational burden, and mutational signatures.

(**a**) Bar graphs showing the percentage of analyzed samples belonging to each B-ALL (top) or T-ALL (bottom) subtype. (**b**) Top, mutational burden in each B-ALL subtype with at least 5 samples. This shows the number of somatic SNVs per megabase (Mb) in each sample (points) sequenced by WES (gray) or WGS (dark gray), with the median indicated by a yellow bar. Beneath this, mutational signatures are shown for each WGS sample in subtypes with at least 3 WGS samples. Signatures are shown as the percentage of SNVs caused by each signature (y-axis), as indicated by colors in the legend at right. Samples in each subtype are sorted by increasing mutation burden from left (low burden) to right (high burden). Bottom shows the number of somatic driver or putative driver alterations per sample, with center indicating mean and whiskers indicating standard deviation. Known/putative driver alterations, detected by WGS, WES, or RNA-seq, are separated into fusions/rearrangements (such as driver fusions and enhancer hijacking events), coding SNVs or indels in putative driver genes, and focal deletions in putative driver genes (tumor suppressors). The sum of all putative driver alterations is also shown (total drivers). If the same gene was affected twice by SNVs, indels, or focal deletions in one sample, it was counted as one alteration. The n values at bottom indicate the number of samples analyzed per subtype for mutation burden (top, samples with WGS or WES), mutational signatures (middle, WGS), or putative driver burden (bottom, WGS or WES plus SNP copy array). (**c**) As in (b), except for T-ALL.

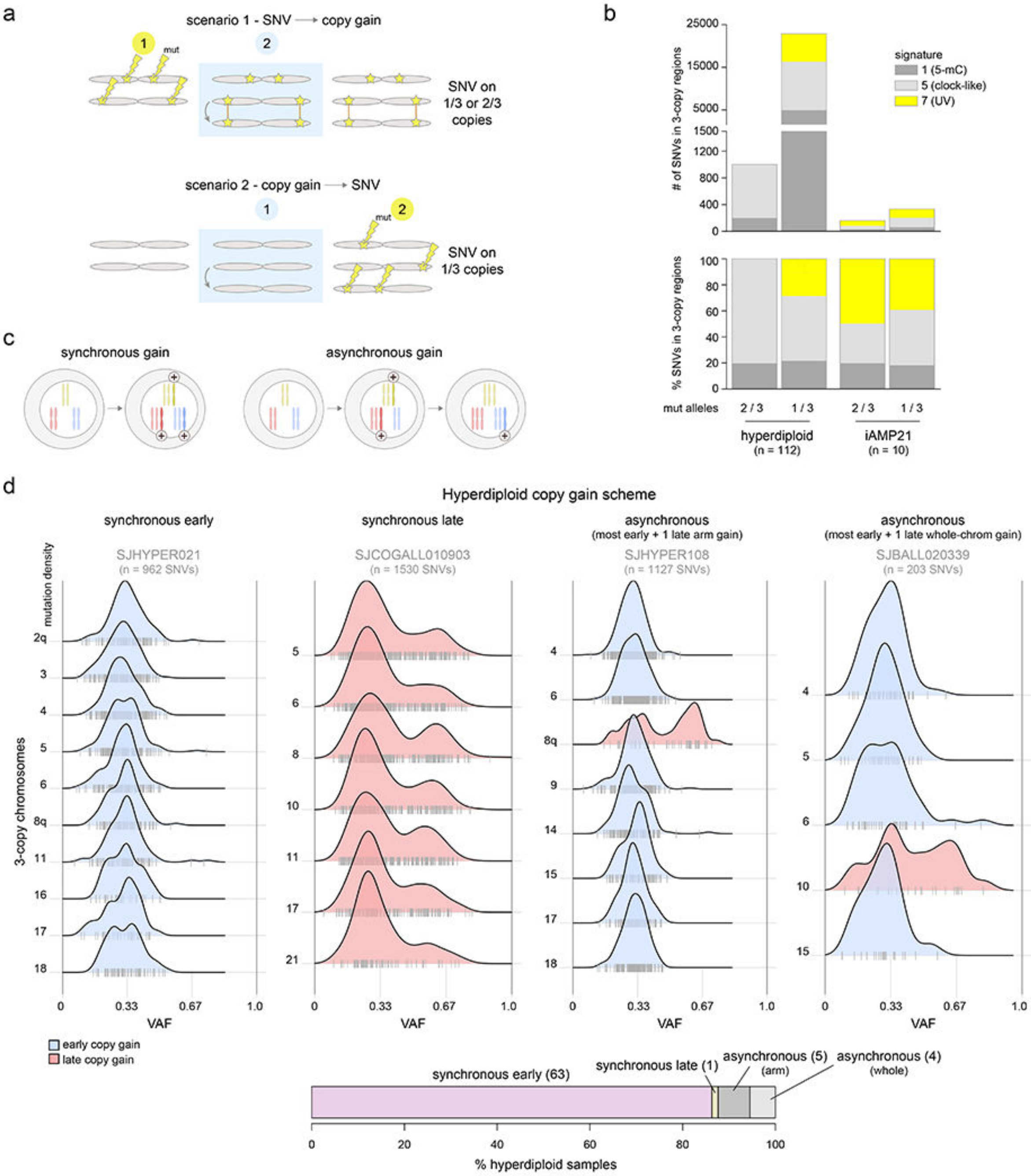

Figure 2. Temporal evolution of ultraviolet-associated mutations and copy gains in aneuploid B-ALL subtypes.

(**a**) Schematic showing how to infer whether copy gains occurred early or late (relative to the occurrence of SNVs). Two homologous chromosomes are shown before (left), during (blue shaded box), and after (right) a somatic gain of one of the two homologs. Top shows a scenario where SNVs (stars) occurred before copy gains, which would lead to half of SNVs being found on 1 of 3 copies and half on 2 of 3 copies, after the gain. Bottom shows a scenario where copy gains happened early, prior to SNVs, and thus all

SNVs occur on 1 of 3 copies. (**b**) Mutational signature analysis pooling all somatic SNVs in 3-copy regions from B-ALL hyperdiploid (n=110 samples) or iAMP21 (n=7) samples (sequenced by WGS), separated into SNVs found on 1 of 3 copies (VAF ≈ 0.33) or 2 of 3 copies (VAF ≈ 0.67; see Methods). Top shows absolute number of SNVs and bottom shows relative number (percentage). (**c**) Scheme showing two possible modes of acquiring copy gains in hyperdiploid ALL. Left shows a scenario where all copy gains occur simultaneously (synchronous), such as during a single aberrant mitosis. Right shows sequential acquisition of copy gains (asynchronous) through multiple copy gain events occurring over time. (**d**) Copy gain schemes in hyperdiploid samples, to test whether copy gains likely occurred simultaneously or sequentially. Top shows examples of the four schemes that were detected across 72 hyperdiploid WGS samples, where only 3-copy chromosomes with at least 20 somatic SNVs in the sample were analyzed, and only samples with two or more chromosomes meeting this criterion were analyzed. On density plots, x-axes show VAF adjusted for tumor purity, and y-axes show mutation density for each 3-copy whole-chromosome or arm gain in the sample. Vertical ticks on the x-axis show individual SNV VAFs; an abundance of VAFs around 0.67 indicates late copy gains since the SNVs occurred prior to the copy gains (2 of 3 copies), while a preponderance of VAFs around 0.33 indicates early copy gains since most SNVs occurred after the copy gains (1 of 3 copies). Blue indicates an inferred early copy gain and red a late copy gain. Bottom shows the percentage of the 72 samples falling into each category. The density profiles for all 72 samples are shown in Extended data fig. 6.

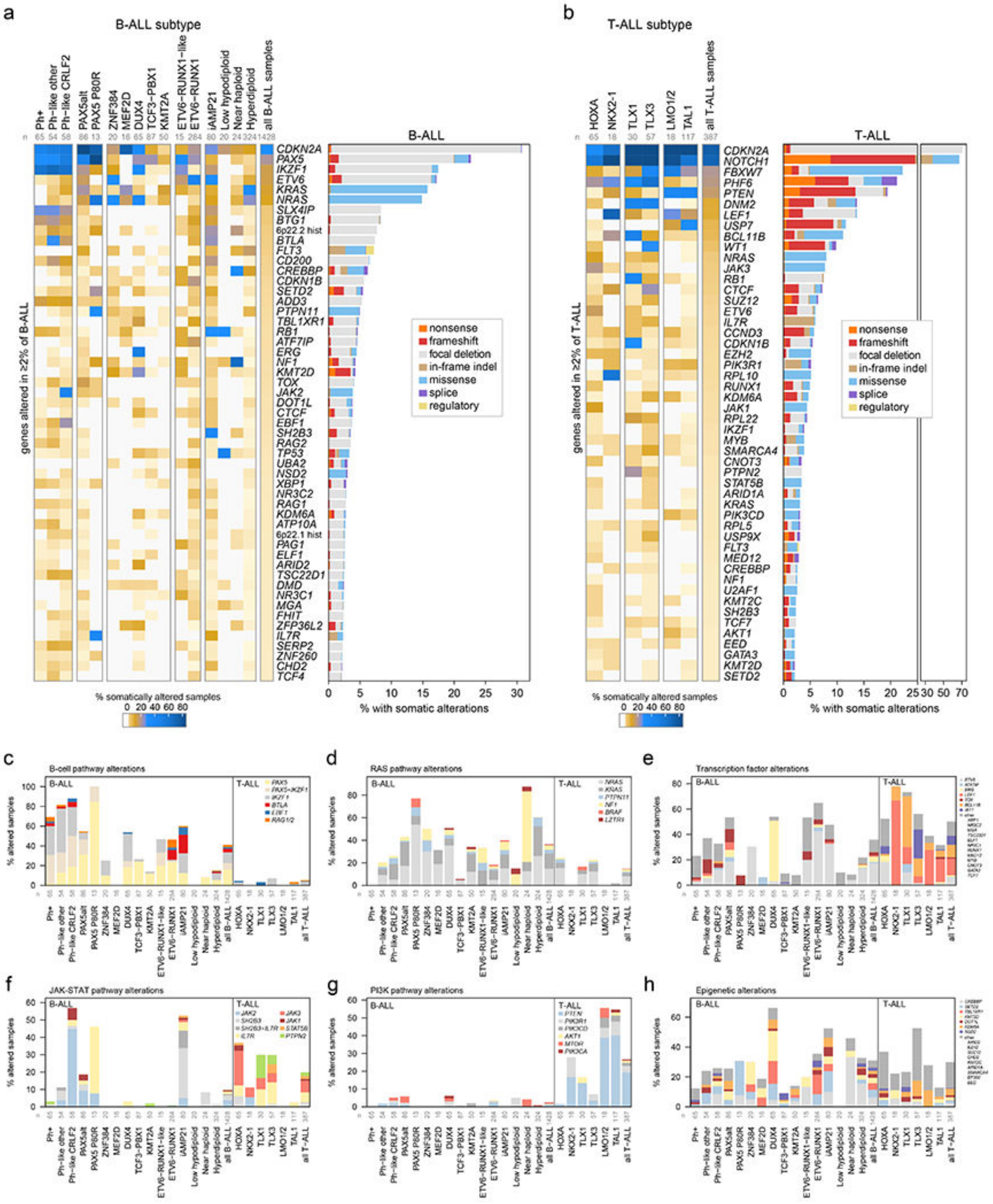

Figure 3. Mutational landscapes across ALL subtypes.

ALL samples with characterization of both somatic SNVs/indels and copy alterations are shown (WGS samples as well as WES samples which also had SNP array analysis), totaling 1,428 B-ALL and 387 T-ALL samples. Subtypes with at least 15 samples are shown. (**a**) Left, heatmap showing the percentage of samples in each subtype (column) with somatic alterations (excluding fusions) in all genes (rows) altered in at least 2% of B-ALL samples. Right shows the percentage of samples with alterations in each gene, with the alteration type indicated by color. In samples with more than one type of alteration, only the alteration higher up in the key list (starting with “nonsense”) is shown. “Regulatory” refers to *FLT3*-region focal deletions thought to increase *FLT3* expression. n below subtype name indicates number of samples analyzed in each subtype. (**b**) As in (a) but for T-ALL. (**c-h**) Percent of samples with somatic alterations (excluding fusions) in each pathway, broken down by subtype. The specific gene altered is indicated in color. In samples where more than one gene is altered in the pathway, the gene towards the top of the legend is only shown. Frequently co-occurring gene alterations are shown as a separate color (e.g. samples with both *PAX5* and *IKZF1* alteration in (c)). Sample numbers for each subtype are as in (a-b).

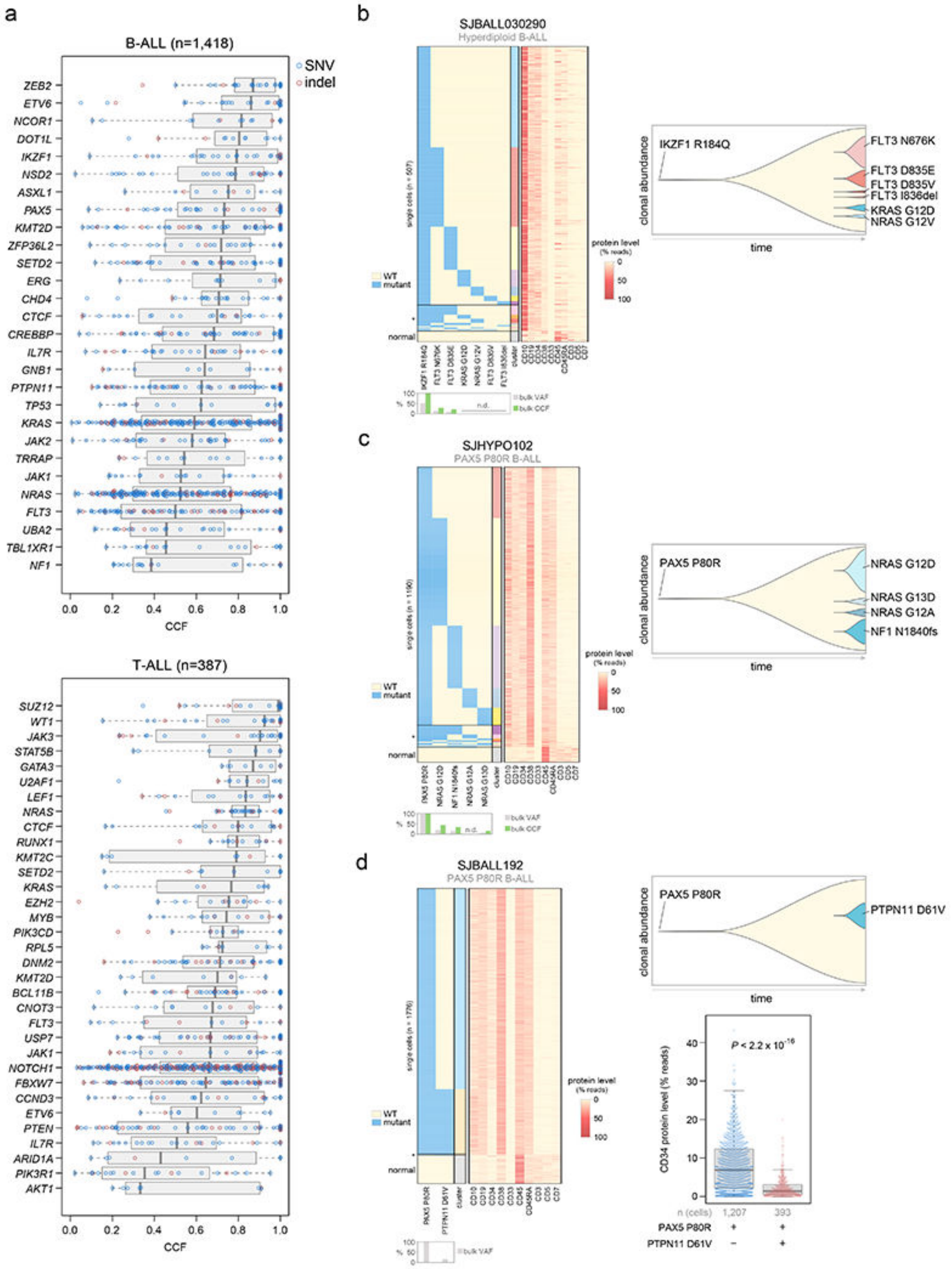

Figure 4. Clonality of driver SNVs and indels.

(**a**) The cancer cell fraction (CCF, x-axis), i.e. the percentage of cancer cells harboring each mutation, of alterations in each driver or putative driver gene is shown in all B-ALL samples (top) or all T-ALL samples (bottom). The CCF was calculated based on the VAF, copy number, and tumor purity of each sample; calculated CCFs above 1.0 were considered 1.0. Samples with both SNV/indel and copy number characterization (WGS or WES plus SNP array) are shown. Each plot shows the number of samples analyzed (n) at top. For most samples, only SNVs/indels in 2-copy regions were analyzed, except for near haploid and low hypodiploid where only SNVs/indels in 1-copy regions were analyzed. SNVs are shown in blue and indels in red; each point represents one somatic mutation. Boxplots show median (thick center line) and interquartile range (box). Whiskers are described in R boxplot documentation (a 1.5*interquartile range rule is used). Known or putative driver genes with at least 10 SNVs/indels in 2-copy regions across all B-ALL samples, or 8 SNVs/indels in 2-copy regions across all T-ALL samples, are shown. (**b-d**) Simultaneous targeted single-cell DNA sequencing and cell-surface protein expression analysis of three B-ALL samples using the Tapestri platform. Left shows a heatmap with each row representing one cell, and each column representing either one mutation (left side) or one protein (right side). Mutation presence is indicated by blue color, while protein level (as a percent of all protein-associated reads detected in the cell) is indicated by red color. Asterisk (*) indicates likely cell doublets or dropout artifacts, and below these likely normal cells are indicated (neither of which were included in the clonal composition determination at right). The bulk VAF of each mutation is indicated below, along with bulk CCF (if copy number was available). n.d., not detected in bulk sequencing. On the right side of each panel is shown a fish plot showing clonal composition as determined by single-cell sequencing, with x-direction indicating time and y-direction indicating relative CCF of each clone (represented by different colors) as determined by single-cell DNA sequencing. The rightmost edge shows the clonal composition at diagnosis. At bottom-right in (d), the cell-surface protein level of CD34 (percent of reads in each cell assigned to CD34), is shown in a clone with vs. without PTPN11 D61V in patient SJBALL192. *P* value is by two-sided Wilcoxon rank-sum test. Boxplot shows median (thick center line) and interquartile range (box). Whiskers are described in R boxplot documentation (a 1.5*interquartile range rule is used).

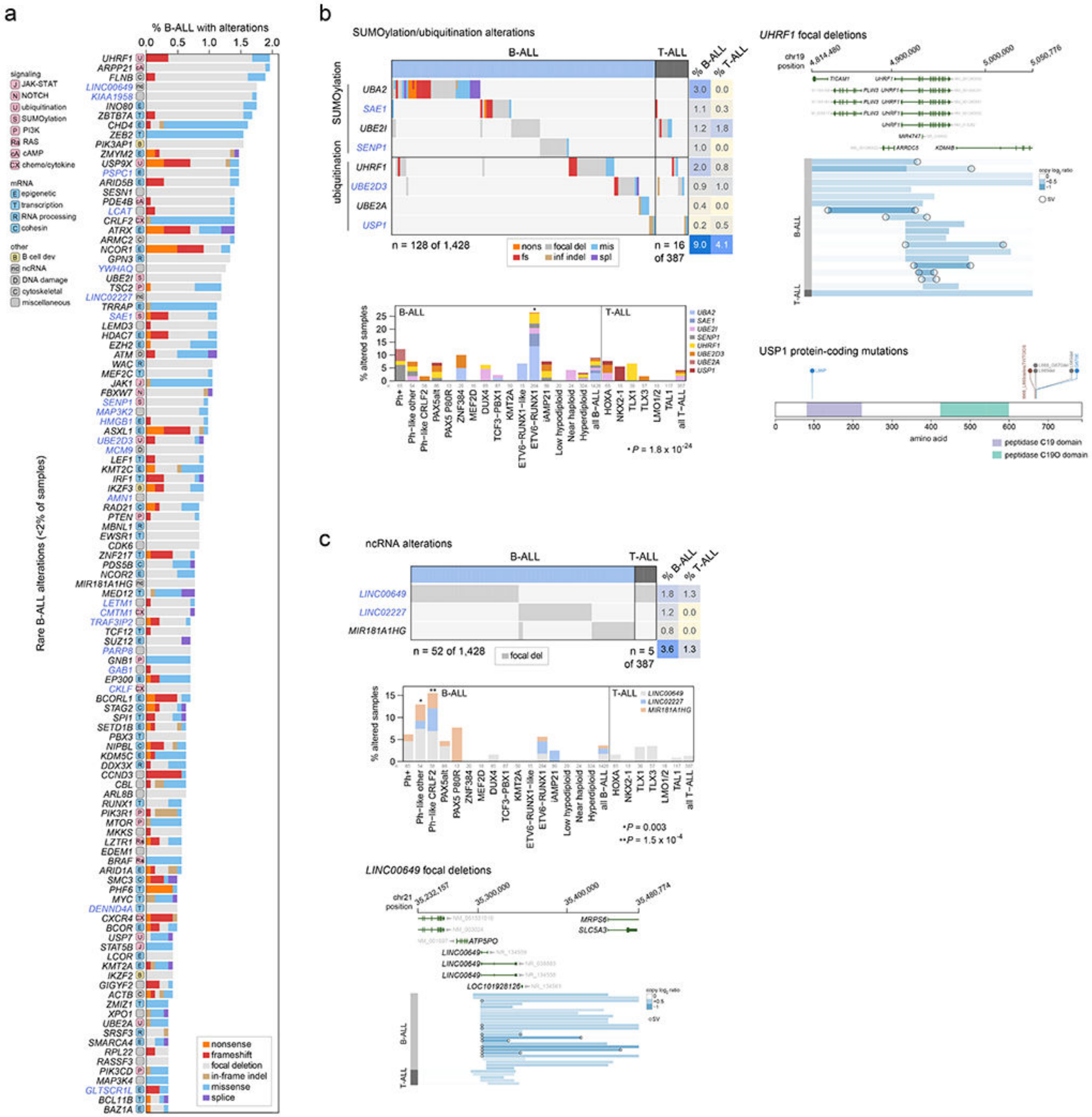

Figure 5. Alterations in rare ALL genes.

(**a**) Percent of B-ALL samples (out of 1,428 with either WGS or WES plus SNP array) with alterations in each infrequently altered gene (altered in <2% of B-ALL samples and ≥0.3% of samples). Alteration type is indicated in color; in samples with more than one type of alteration, only the alteration higher up in the key list (starting with “nonsense”) is shown. Putative driver genes not previously reported in cancer are shown in blue text. The pathway or function of each gene is indicated in boxed letters above each gene (see legend at bottom). (**b**) Alterations in selected genes involved in SUMOylation or ubiquitination, or the removal of these modifications. Left shows an oncoprint showing only samples with alterations in at least one of these genes, with alteration indicated by color and the percentage of samples in B-ALL or T-ALL altered at right. Bottom-left shows the percentage of each subtype with alterations in these genes, color-coded by the specific gene altered. In samples with alterations in more than one gene, only the top-most gene in the legend is shown. The value of n indicates the number of samples analyzed in each subtype. Right shows example gene alterations, including focal deletions (5 Mb or less; blue indicates degree of copy loss in each sample (row) and circles indicate SVs which were available for WGS samples only) in *UHRF1* and sequence alterations in *USP1*. *P* value (asterisk) is by two-sided Fisher's exact test comparing prevalence in the *ETV6-RUNX1* subtype vs. all non-*ETV6-RUNX1* B-ALL samples. (**c**) As in (b) but for putative driver alterations in non-coding RNA genes. *P* values (asterisks) are by two-sided Fisher's exact test comparing prevalence in the indicated subtype vs. all B-ALL samples not belonging to that subtype.

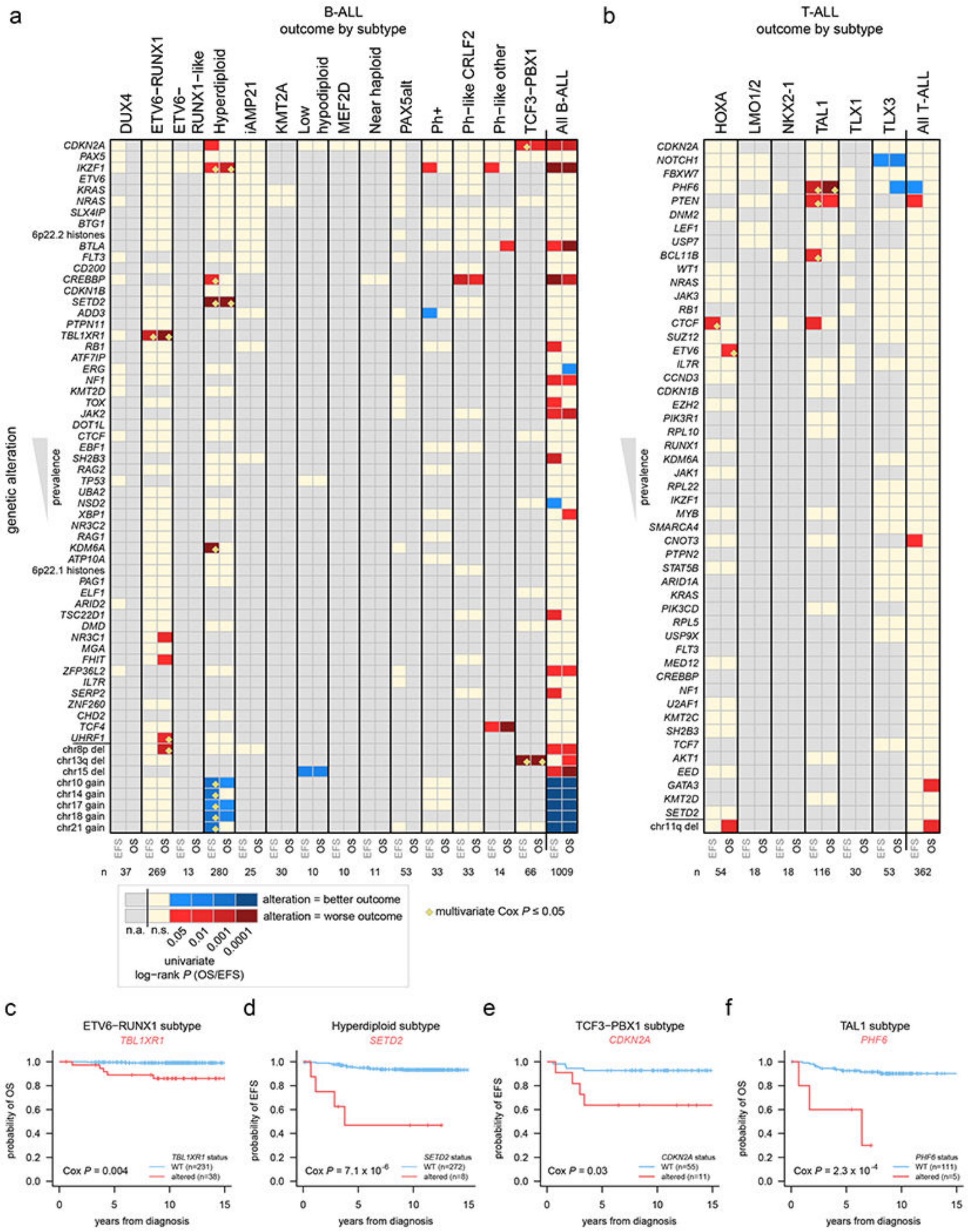

Figure 6. Association of secondary genetic alterations with outcome.

(**a**) Heatmap showing overall survival (OS) and event-free survival (EFS) in each B-ALL subtype based on the presence of specific somatic alterations. Each row represents a specific gene somatically altered, sorted by most frequently altered in B-ALL (top) to least frequently altered (bottom). The bottom-most portion shows selected large copy gains and losses (not sorted by frequency) based on their significant association with outcome. Columns represent B-ALL subtypes, and EFS (left) and OS (right) were analyzed for each subtype. *P* values were first calculated by univariate two-sided log-rank test, and significant

(0.05 or less) values are shown in red (if alteration was associated with worse outcome) or blue (alteration associated with improved outcome; see scale at bottom). Tan color indicates a *P* value that was not significant (n.s.), and gray indicates an insufficient number of somatically altered samples in the subtype for analysis (n.a.; at least 3 altered and 3 wild-type samples were required for the gene to be analyzed within the subtype; at least two samples had to have events (death, relapse, etc.) in the wild-type or altered group as well). Significant associations ($P \leq 0.05$ by univariate analysis) were then subject to multivariate Cox proportional-hazards analysis (Methods) and associations with $P \leq 0.05$ by this multivariate method are marked by yellow diamonds (not performed for the "all B-ALL" and "all T-ALL" analyses). The number of samples analyzed in each subtype is indicated at bottom and includes samples with SNV/indel and copy data (WGS, or WES plus SNP copy array) and available outcome information. All B-ALL samples, regardless of subtype, were also analyzed in the rightmost heatmap column. (**b**) Heatmap showing OS and EFS in each T-ALL subtype based on somatic alterations, similar to panel (a) but for T-ALL. (**c-f**) Kaplan-Meier OS or EFS curves showing selected genetic alterations with significant outcome associations within indicated subtypes. *P* values are by multivariate Cox proportional-hazards analysis.

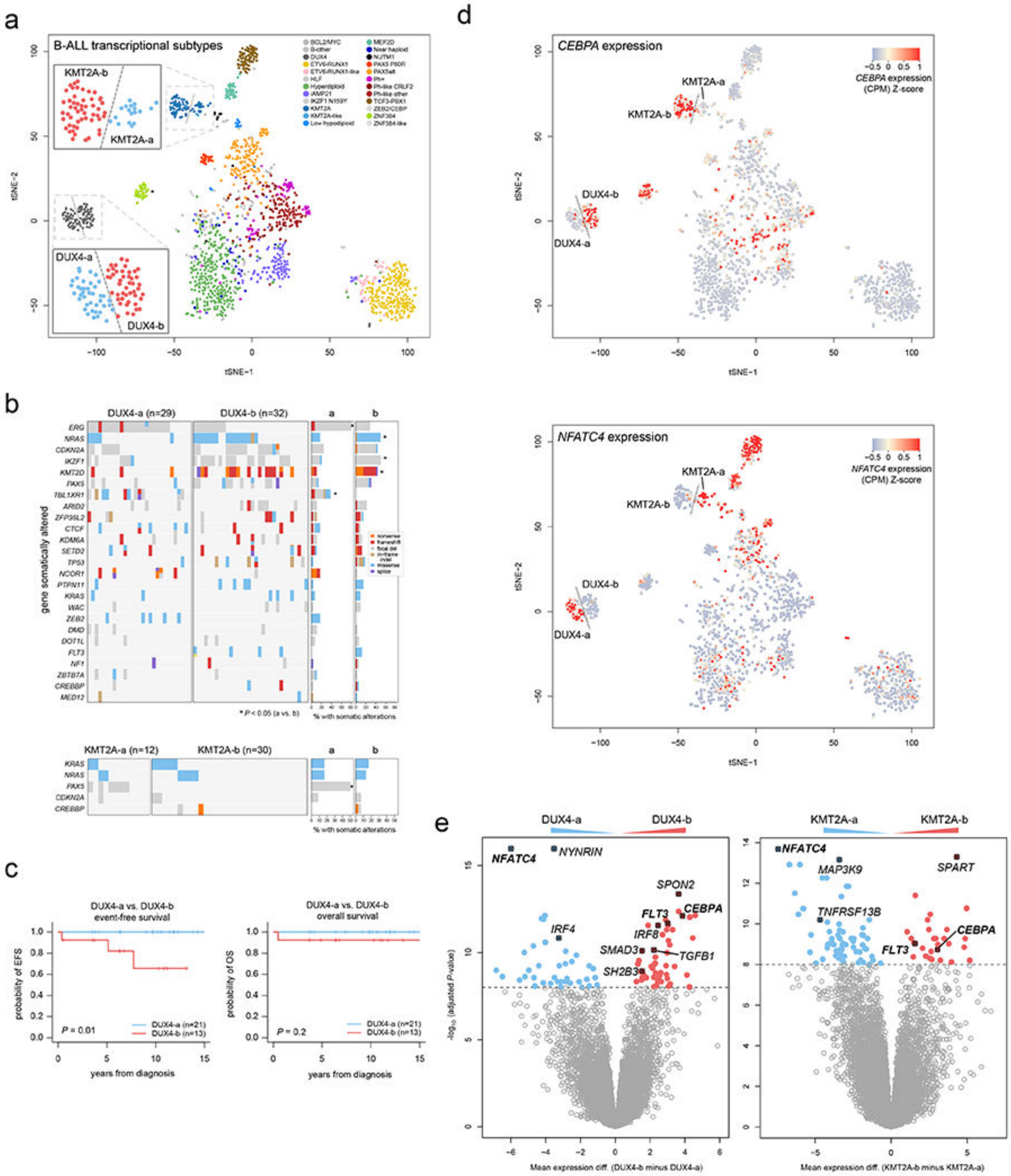

Figure 7. Dichotomous *CEBPA* and *NFATC4* expression identifies subgroups of *KMT2A*-and *DUX4*-rearranged subtypes.

(**a**) tSNE analysis of B-ALL transcriptional profiles including 1,464 B-ALL samples sequenced by RNA-seq. Each point represents one sample. Legend shows the samples colored by subtype, and dotted lines delineate visually apparent subgroups further subdividing the *KMT2A* and *DUX4* subtypes. Zoomed-in regions showing *DUX4*-a vs. *DUX4*-b and *KMT2A*-a vs. *KMT2A*-b subgroups are shown. (**b**) Heatmaps showing mutations present in *DUX4*-a vs. *DUX4*-b (top), or *KMT2A*-a vs. *KMT2A*-b (bottom) subgroups. Each row indicates a gene somatically altered in the subtype, sorted by most frequently (top) to least frequently (bottom) altered within the *DUX4* or *KMT2A* subtype. Each column is one sample. Right indicates the percentage of samples with somatic alterations in each gene in the a vs. b subgroups, with significant *P* values by two-sided Fisher's exact test (a vs. b subgroups) shown with asterisks. Exact *P* values are 9.3 x 10^{-5} (*ERG*), 0.014 (*NRAS*), 0.032 (*IKZF1*), 0.0045 (*KMT2D*), 8.3 x 10^{-5} (*TBL1XR1*), and 1.8 x 10^{-4} (*PAX5*). Variant types are indicated by color as shown in the key at right in the *DUX4* plot. This analysis includes samples that had RNA-seq, SNV/indel, and copy number characterisation (RNA-seq plus WGS, or RNA-seq plus WES plus SNP array), with sample numbers indicated above each plot. (**c**) Kaplan-Meier curves showing event-free (left) or overall survival comparing *DUX4*-a and *DUX4*-b subgroups. *P* values are by two-sided log-rank test. (**d**) tSNE plots as in (a), including 1,464 B-ALL samples, except that the expression of *CEBPA* (top) or *NFATC4* (bottom) are indicated by color, with red indicating high expression and blue/gray indicating lower expression (see scale). (**e**) Left, differential gene expression with Limma, comparing the *DUX4*-a (n=36 samples) and *DUX4*-b (n=43) subgroups, defined as shown in (a). X-axis represents the $\log_2$ fold change in gene expression comparing *DUX4*-b minus *DUX4*-a, where values above zero indicate an increase in *DUX4*-b and below zero indicate an increase in *DUX4*-a. Y-axis represents the $-1*\log_{10}$ (adjusted *P* value) for each gene (represented as points). The top differentially expressed genes are shown in red (increased in *DUX4*-b) or blue (increased in *DUX4*-a), and selected genes are highlighted. Right, differential gene expression comparing *KMT2A*-a (n=17) vs. *KMT2A*-b (n=45).